

GECO: Galaxy Evolution COde – A new semi-analytical model of galaxy formation

E. Ricciardelli^{1,2,3} and A. Franceschini¹

¹ Dipartimento di Astronomia, Università di Padova, vicolo Osservatorio 2, 35122 Padova, Italy
e-mail: elenaricci@iac.es

² Instituto de Astrofísica de Canarias, vía Lactea s/n, 38200 La Laguna, Tenerife, Spain

³ Departamento de Astrofísica, Universidad de La Laguna, 38205 Tenerife, Spain

Received 29 September 2009 / Accepted 16 April 2010

ABSTRACT

Aims. We present a new semi-analytical model of galaxy formation, GECO (Galaxy Evolution COde), designed to improve our understanding of when and how the processes of both star formation and galaxy assembly took place, by comparison with a wide variety of data about galaxy mass-function evolution and star-formation histories.

Methods. Our model is structured into a Monte Carlo algorithm based on the extended Press-Schechter theory, to represent the merging hierarchy of dark matter halos, and a set of analytic algorithms to treat the baryonic physics, including classical recipes for gas cooling, star-formation timescales, galaxy mergers, and supernova (SN) feedback. In addition to the galaxies, the parallel growth of BHs is followed in time, and their feedback on the hosting galaxies is modelled. We set the model free parameters by matching data on local stellar mass functions and the relation between galaxy bulge and black-hole mass at $z = 0$.

Results. Based on these local boundary conditions, we investigate how data on the high-redshift universe constrain our understanding of the physical processes driving the evolution, focusing in particular on the assembly of stellar mass and the star-formation history of galaxies. Since both processes are currently strongly constrained by cosmological near- and far-IR surveys with the Spitzer Space Telescope, the basic physics of the Λ CDM hierarchical clustering concept of galaxy formation can be effectively tested by us by comparison with the most reliable set of observables using a minimal number of free parameters.

Conclusions. Our investigation shows that when the timescales of star formation and mass assembly are studied as a function of dark matter halo mass and a given galaxy stellar mass, the “downsizing” fashion of star formation appears to be a natural outcome of the model, being reproduced even in the absence of the AGN feedback. In contrast, the stellar mass assembly history turns out to follow a more standard hierarchical pattern that is progressive with cosmic time, the more massive systems being assembled at later times mainly through dissipationless mergers.

Key words. galaxies: evolution – galaxies: formation – galaxies: halos

1. Introduction

Several pieces of observational evidences have accumulated that favour the Λ CDM paradigm for structure formation, which is now quite a successful rendition of the hierarchical clustering scenario for cosmic structure formation. In its standard form (Blumenthal et al. 1984), it predicts that structures formed from primordial fluctuations of the density field that were amplified during inflation and then collapsed to form the virialized structures that we see today. The most compelling support for this paradigm has been the measurements of the temperature anisotropies of the cosmic microwave background (Spergel et al. 2003, 2007). Additional evidence has included the measurements of the power spectrum of galaxy clustering from large surveys of the local universe (Percival et al. 2002; Tegmark et al. 2004), the evidence of an accelerated expansion of the universe as inferred from high-redshift type Ia supernovae observations (Riess et al. 1998; Perlmutter et al. 1999), and the baryon fraction observed in rich clusters (White et al. 1993).

Devised to study galaxy evolution within this cosmological framework, the semi-analytical approach involves a relatively simple handling of the main physical parameters and

understanding of their possible role in driving the evolution. This modelling has its root in the work of White & Rees (1978), where it was proposed that galaxy formation is a two-stage process, with dark matter halos forming in a dissipationless gravitational collapse and galaxies forming inside them following the radiative cooling of baryons. Although White & Rees (1978), and afterwards, White & Frenk (1991), based their work only on the analytic Press-Schechter theory (Press & Schechter 1974), predicting only average quantities, subsequently a number of works followed their prescriptions using Monte Carlo (MC) merger trees. The MC approach allows to obtain several realizations of the merging history of individual dark matter halos. This approach was pioneered by Lacey & Cole (1993), Kauffmann & White (1993), Cole et al. (1994), and then followed by a number of authors (Somerville & Kolatt 1999; Sheth & Lemson 1999; Zentner 2007). The great advantage of the semi-analytical method (SAM), apart from being computationally very fast and flexible, is that it is possible to compute merging histories with arbitrary mass resolution. The alternative means of tracking the evolution of the dark matter halos, is through the use of large-scale cosmological N -body simulations, whose far greater computational requirements are compensated by the

amount of information that can be achieved. For instance, in the Millennium Simulation (Springel et al. 2001), the evolution of substructures in massive halos can be followed in time, providing more detailed information about the galaxy dynamics and the influence of the cosmic environment on the process (De Lucia et al. 2004). In the literature, various examples of this “hybrid” approach, which use N -body simulations to model the dark matter evolution and the SAM technique for the baryonic physics, have been published (Hatton et al. 2003; De Lucia et al. 2006; Croton et al. 2006).

In the present work, we employ a MC merger tree, mainly because this allowed us to test the parameter space of the semi-analytical model with far more flexibility than using N -body simulations, and allows to compute merging histories down to arbitrarily low mass resolution.

While the treatment of the evolution of dark matter structures is relatively simple, being determined only by gravity, the physics of the baryons inside halos is much more complex to describe. In the most classical models (Kauffmann et al. 1993; Baugh et al. 1996; Kauffmann et al. 1999; Somerville & Primack 1999; Cole et al. 2000; Menci & Cavaliere 2002), gas cooling, star formation, supernova (SN) feedback, and galaxy mergers are included. It has become clear that some other form of highly energetic feedback is needed to prevent star formation in massive galaxies at recent epochs, where the SN feedback is ineffective. The need of such form of feedback is required in order to avoid the overcooling in massive halos, and hence the overabundance of galaxies at the bright-end of the luminosity function. This source of feedback is commonly found in the AGN energy production. This effect, supported by the observational findings of a tight correlation between the BH and the bulge size (Ferrarese & Merritt 2000; Häring & Rix 2004), was implemented in different ways by Kauffmann & Haehnelt (2000), Bower et al. (2006), Croton et al. (2006), Menci et al. (2006), Somerville et al. (2008).

As an alternative to AGN feedback, the shutdown of star formation above a critical halo mass has been implemented as a quenching mechanism in massive galaxies (Cattaneo et al. 2006, 2008), motivated by the prediction of stable shock heating for halos more massive than this threshold (Dekel & Birnboim 2006).

Following the prescriptions of these models, we have compiled a new semi-analytical model, the Galaxy Evolution COde (GECO), whose aim is to identify a few key physical parameters and modify them by comparing with several basic properties of the galaxy population at $z = 0$, as well as at high redshifts. Our main observational reference in this paper is the redshift-dependent stellar mass function of galaxies, which, for a suitable choice for the stellar initial mass function (IMF), is a robust descriptor of the star formation history and the mass assembly history of galaxies.

The structure of the paper is as follows. In Sect. 2, we describe the Monte Carlo merger tree used in the model. In Sect. 3, we introduce the ingredients of the baryonic model. In Sect. 4, we explain how the free parameters are set and provide a table for them. In Sect. 5 the basic results for the local universe are presented, while in Sect. 6 we focus on the high redshift predictions. We conclude in Sect. 7. Throughout the rest of the paper we assume a “concordance” cosmological model, with $\Omega_m = 0.3$, $\Omega_\Lambda = 0.7$, $h = 0.7$, $\sigma_8 = 0.9$ and $n = 1$ (power index of the primordial power spectrum). However, when needed, we also show the dependence on the cosmological parameters by considering the results for the latest WMAP5 dataset, which are

$\Omega_m = 0.258$, $\Omega_\Lambda = 0.742$, $h = 0.719$, $\sigma_8 = 0.796$, and $n = 0.963$ (Dunkley et al. 2009).

2. Merger tree

2.1. The formalism

In the hierarchical theory of structure formation the density contrast $\delta = (\rho - \rho_b)/\rho_b$, where ρ_b is the mean density of the universe and ρ is the perturbation density, is a Gaussian random field that at early times grows linearly. When the density contrast reaches a critical value δ_c , given by the spherical collapse theory, the perturbation begins to collapse and form virialized halos. To associate masses with these collapsed objects, the Press-Schechter approach considers the fluctuations whose density contrast smoothed on a scale R_M , through a spatial window function $W(r, R_M)$, exceeds δ_c .

The Gaussian random variable δ has a zero mean and a variance $S(M) = \sigma^2(M)$ that is linked to the mass by means of the power-spectrum $P(k)$

$$\sigma^2(M) = \frac{1}{2\pi^2} \int P(k)W^2(kr)k^2 dk, \quad (1)$$

where $W^2(kr)$ is the Fourier transform of the spatial window function. In the excursion-set approach, developed by Bond et al. (1991), the value of δ executes a random walk as the smoothing scale R_M (or M) is changed. We can consider the trajectories in the plane (S, δ_c) and associate the fraction of matter in collapsed objects in the range dM around M at the time t , with the fraction of trajectories that make the first upcrossing through the threshold δ_c in the interval $S, S + dS$. This results in the well-known PS mass function

$$f(S, \delta_c)dS = \frac{1}{\sqrt{2\pi}} \frac{\delta_c}{S^{3/2}} \exp\left(-\frac{\delta_c^2}{2S}\right) dS \quad (2)$$

(Press & Schechter 1974).

In the *Extended Press-Schechter* model (Bond et al. 1991; Lacey & Cole 1993), it is also possible to derive the conditional mass function, the fraction of trajectories in halos with mass M_1 at z_1 that are in halos with mass $M_0 > M_1$ at $z_0 < z_1$:

$$f(S_1, \delta_{c1}|S_0, \delta_{c0})dS_1 = \frac{1}{\sqrt{2\pi}} \frac{(\delta_{c1} - \delta_{c0})}{(S_1 - S_0)^{3/2}} \exp\left[-\frac{(\delta_{c1} - \delta_{c0})^2}{2(S_1 - S_0)}\right] dS_1. \quad (3)$$

Converting mass weighting in number weighting, we obtain the average number of progenitors at z_1 in the mass interval dM_1 around M_1 that at redshift z_0 has merged to form an M_0 halo:

$$\frac{dP}{dM_1}(M_1, z_1|M_0, z_0)dM_1 = \frac{M_0}{M_1} f(S_1, \delta_{c1}|S_0, \delta_{c0}) \left| \frac{dS}{dM} \right| dM_1. \quad (4)$$

2.2. The partition algorithm

To generate Monte Carlo realizations of the merging history of dark matter halos, we use the partition algorithm described by Sheth & Lemson (1999), hereafter SL99, which is exact for a white-noise power-spectrum, but needs some modifications to be applied to a Λ CDM fluctuation spectrum. Since we will describe in detail both the algorithm and the test performed to probe its consistency in a separate paper, we provide only a brief description here.

The algorithm is based on the assumption that for a white-noise spectrum mutually disconnected volumes are mutually

independent, as analytically demonstrated in the Appendix of SL99. We refer to as a *parent* the halo of mass M_0 that exists at $z = 0$ and *progenitors* its smaller constituents at higher redshift. We partition a halo of mass M_0 into progenitors by choosing first one progenitor and then another from the remaining mass and so on until the remaining mass falls below a certain minimum mass given by our mass resolution M_{res} . We have a probability of finding the first progenitor of mass M_1 , corresponding to S_1 , given by $f(S_1, \delta_{c1}|S_0, \delta_{c0})$ (Eq. (3)) and we choose a mass by drawing a random number from this distribution. We can consider the halo M_0 to be a region of size $V_{M_0} = M_0 b_0 / \rho_b$, where $b_0 = 1/(1 + \delta_0)$. If the first progenitor has mass M_1 , it occupies a volume $V_{M_1} = M_1 b_1 / \rho_b$. The remaining mass $R = M_0 - M_1$ is distributed in the volume $V_R = R b_R / \rho_b$, hence, for the conservation of volumes, the density in this region is given by

$$\delta_{cR} = \delta_{c1} - \frac{(\delta_{c1} - \delta_{c0})}{1 - (M_1/M_0)} \quad (5)$$

to lowest order in δ (see Eq. (5) of SL99). The second progenitor must then be chosen from the remaining mass R and the probability that it has mass M_2 , corresponding to S_2 , is given by $f(S_2, \delta_{c2}|S(R), \delta_{cR})$. We therefore choose a random number from this distribution. We then iterate the process by continuing to find progenitors until the remaining mass is below the mass resolution.

The assumption that disconnected volumes are mutually independent is correct only for white noise power spectrum, but we wish to build merger trees for a Λ CDM spectrum. SL99 show that applying the same algorithm to scale-free spectra with $n \neq 0$ leads to inconsistencies in the excursion set mean values. Since we know that all the excursion set quantities are independent of the power spectrum when they are expressed in terms of the variance rather than the mass, we run the algorithm for the white-noise case. We then consider each chosen M_{wn} not as a progenitor with mass M_{wn} , but as a region populated by some number ν of objects with mass $M_{\Lambda\text{CDM}}$. In practice, we normalize the white-noise power spectrum in such a way that the mass variance of the two spectra is the same in M_0 , i.e. $S_0 = S_{\Lambda\text{CDM}}(M_0)$. We then choose S_1 from the distribution of Eq. (3). We associate this variance with a mass given by the white-noise spectrum $M_{\text{wn}} = S_0 M_0 / S_1$ and one given by the Λ CDM spectrum $M_{\Lambda\text{CDM}}$. We consider a number ν of halos with this mass, given by $\nu = M_{\text{wn}} / M_{\Lambda\text{CDM}}$, approximated to the nearest integer. We then iterate the procedure for each new progenitor.

As a test of the consistency of our MC merger tree with the PS predictions, in Fig. 1 we show the global mass function of dark matter halos. To compute it, we use a grid of 35 parent halo masses, ranging from $10^{10} M_\odot$ to $10^{15} M_\odot$, logarithmically spaced, and simulate 100 realizations for each parent halo. We then weight each halo with the PS number density at $z = 0$. The results do not depend much on the number of parent halo masses used, but are quite sensitive to the number of realizations for each halo. The 100 realizations used are found to be a good compromise between the good sampling desired and the computational time required. We compiled a grid in time of 52 intervals logarithmically spaced in redshift, ranging from $z = 20$ when the time-step is approximately equal to 0.05 Gyr to $z = 0$ with a ~ 0.8 Gyr time-step. Because our method for building a merger tree is insensitive to the time-step used, the choice of the time-step grid is quite arbitrary and we do not have to use too small time intervals. We find very good agreement between the MC method and the analytical predictions. A key point of this algorithm is that it correctly reproduces the mean statistical quantities of EPS and PS predictions for any set of M_1, z_1, M_0, z_0 . This

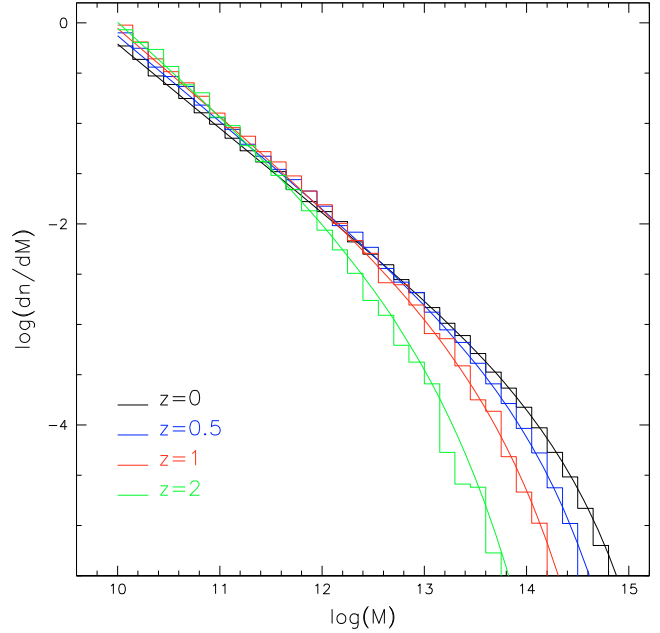


Fig. 1. Global mass function for dark matter halos at different redshifts. Histograms represent the mass function derived from our MC merger tree, while solid lines show the PS predictions.

means that there is no need to divide the time interval between z_0 and z_1 into smaller time-steps. This is particularly convenient because it allows us to choose the time grid for the semi-analytical implementation in an arbitrary way.

The algorithm described is based on the extended Press-Schechter formalism, which is based on the spherical barrier model, but can be extended to a more general moving barrier model, such as the ellipsoidal collapse model (Bond & Myers 1996) which more closely resembles the results from N -body simulations (Sheth & Tormen 2002; Giocoli et al. 2007; Zentner 2007; Zhang et al. 2008).

3. The baryonic model

While the theory of the hierarchical development of the dark matter structures is relatively simple and now well established, the complex physics of baryons remain uncertain, and requires the treatment of several processes in a simplified form. The latter is obtained with the introduction of a minimum number of free parameters in the model, which can only be defined by comparing the model predictions with observational data. These parameters represent our lack of knowledge about the details of the physics of galaxy formation. Although they are defined by fitting model results with observations, only limited ranges of values are allowed: values outside these would indicate fundamental problems in the process treatment or lack of important physical ingredients. This section is dedicated to a description of our new SAM model, GECO.

At variance with the majority of the models of galaxy formation, we tested our results directly on the observables involving stellar mass rather than luminosities, to avoid introducing further uncertainties in the model due to the spectrophotometric synthesis, dust extinction, and the initial mass function. The elaboration of the photometric synthesis based on the model galaxy mass function will be deferred to a future work.

3.1. Linking galaxies to dark matter halos

As described in the previous section, the generation of the merger tree proceeds backwards in time. Starting from the initial redshift (typically $z = 0$), we split each halo into progenitors at higher redshifts. In contrast, galaxy formation is modelled forward in time, starting from the “leaves” of the tree, i.e., halos at high redshift whose progenitors fall below the mass limit resolution ($M_{\text{res}} = 10^{10} M_{\odot}$ in our case) and their hierarchy is not followed any further in time. Starting from each of these halo, we place baryons inside them, according to the baryonic fraction observed by WMAP5 of $f_b = \Omega_b/\Omega_m = 0.17$ (Dunkley et al. 2009).

We use the grid in parent halo masses and time-steps described in Sect. 2.2. To solve the differential equations for baryon evolution that we are going to introduce in the following sections, we divide each step of the merger hierarchy into 100 smaller substeps which allow us to solve the system of equations through the use of finite increments of mass.

To derive statistical quantities such as the mass function or the SFR density, we simply make a weighted sum over the model galaxies. Since we are dealing with an EPS merger tree, we use for consistency as a weight scheme the number density of halos given by the PS mass function. In some cases, we have also checked the results using a Sheth & Tormen number density (Sheth & Tormen 2002), which fits the results of N -body simulations with higher accuracy, but we have found that it makes little difference.

We will describe in the following the baryonic processes at work in driving the evolution of galaxies, starting from the cooling of the gas.

3.2. Dynamical timescales and gas cooling

The cooling of the gas is a fundamental process of galaxy formation, because it defines the rate at which gas becomes available for star formation. The first to invoke the need for some form of dissipative process occurring inside dark matter halos were White & Rees (1978), to explain the difference between the luminosity function of galaxies, with its characteristic mass and size, and the halo mass function, which on galactic scales is a typical power law without any preferred scales. White & Rees argued that galaxy formation is a two-stage process, with dark matter halos forming by means of the dissipationless hierarchical clustering, and gas cooling then occurring inside them.

The gas is assumed to be heated by shocks during the violent relaxation following the collapse, to the virial temperature of the halo, given by

$$T = \frac{1}{2} \frac{\mu m_{\text{H}}}{k} V_{\text{c}}^2, \quad (6)$$

where μ is the mean molecular mass of the gas, m_{H} is the mass of a hydrogen atom, k is the Boltzmann’s constant, and V_{c} is the circular velocity of the halo, which can be related to the mass of the halo by the expression $V_{\text{c}} = \sqrt{GM_{\text{halo}}/R_{\text{vir}}}$. The virial radius, R_{vir} , is the limiting radius of a virial halo, within which the mean density is $200\rho_{\text{c}}$, where ρ_{c} is the universal critical density, given by $R_{\text{vir}} = 1.63 \times 10^{-2} (M_{\text{halo}}/M_{\odot} h^{-1})^{1/3} (\Omega(z)/\Omega_{\text{m}})^{1/3} (1+z)^{-1} h^{-1}$ kpc (Navarro et al. 1997). From V_{c} and the virial radius R_{vir} , a halo dynamical time can be defined to be

$$t_{\text{halo}} = R_{\text{vir}}/V_{\text{c}}. \quad (7)$$

The rate at which the gas cools depends upon both this temperature, which determines its ionization state, and the metallicity

of the gas, which defines its chemical composition. We consider the cooling function $\Lambda(T, Z)$ tabulated by Sutherland & Dopita (1993). We note that the cooling function also depends on the metallicity of the hot gas: higher metallicities cause higher cooling rates, because of line cooling from heavy elements, mainly for low-mass halos. We assume that the hot gas has a metallicity that is constant and equal to $0.3 Z_{\odot}$, close to the value for the hot gas in cluster (Somerville et al. 2008). We also checked that by adopting a solar metallicity instead of the subsolar one, the results do not change significantly.

The cooling time is defined as the thermal energy density divided by the cooling rate per unit volume

$$t_{\text{cool}} = \frac{3}{2} \frac{\mu m_{\text{H}} k T}{\Lambda(T, Z) \rho_{\text{gas}}}, \quad (8)$$

where ρ_{gas} is the gas density profile, which is assumed to be isothermal and be given by

$$\rho_{\text{gas}}(r) = \frac{M_{\text{hot}}}{4\pi R_{\text{vir}} r^2}, \quad (9)$$

where M_{hot} is the total gas mass in the hot component, which is assumed to extend to the virial radius. A cooling radius, r_{cool} , can now be defined as the point where the local cooling time is equal to the age of the universe at that epoch.

We can now compute the rate at which gas accretes to the centre of the halo, becoming available for star formation. Following the treatment of White & Frenk (1991), we distinguish two regimes of cooling, depending on the value of r_{cool} . The first case corresponds to $r_{\text{cool}} > R_{\text{vir}}$, the cooling radius lying outside the virialized region of the halo. The cooling is so rapid that the infalling gas never reaches the hydrostatic equilibrium and the supply of cold gas for star formation is limited by the infall rate rather than the cooling rate. We assume that all the hot gas in the halo settles to the centre in a timescale given by the halo dynamical time

$$\dot{M}_{\text{cool}} = \frac{M_{\text{hot}} V_{\text{c}}}{R_{\text{vir}}}. \quad (10)$$

This regime of cooling was called the *rapid cooling regime* by White & Frenk (1991), also known as the *cold mode*.

The second infalling method is the static hot halo regime, or *hot mode*, that occurs when the cooling radius lies inside the virial radius. In this case, the gas inside r_{cool} is pressure-supported and contracts quasi-statically toward the centre. Cooling will cause a flow of gas toward the centre in a way exactly analogous to the cooling flow occurring in galaxy clusters. A simple expression for the infall rate is given by

$$\dot{M}_{\text{cool}} = 4\pi \rho_{\text{gas}} r_{\text{cool}}^2 \frac{dr_{\text{cool}}}{dt}. \quad (11)$$

We note that for small halos, which we find preferentially at early times, the cooling radius is greater than the virial radius, and we are in the *cold mode* regime, where Eq. (10) applies. At late times, for large values of the virial velocity, the cooling radius falls below the virial radius and we are in the *hot mode* regime. As a consequence, at high redshift we experience a more efficient cooling. Hydrodynamical simulations, such as that of Kereš et al. (2005), justify the use of two different modes of cooling. They indeed found that a cold mode dominates for low-mass objects, which are found at high redshift or in low-density environments in the nearby universe, while the hot mode contributes significantly for high-mass systems, therefore being

important only at low redshift. We note that in our model the cooling at high redshift may be enhanced due to the assumption of a constant metallicity. In the case of a metal-dependent cooling rate, we would obtain a lower amount of cooling in the high redshift objects with primordial metallicity. We will test such effect in a future version of the code, where the chemical evolution model will be implemented.

3.3. Galaxy sizes and angular momentum

Since several timescales involved in the analytic treatment of galaxy formation (such as for example the star formation rate) that we introduce in the following sections, depend on the dynamical time of the galactic disc ($t_{\text{dyn}} = r_{\text{disc}}/v_{\text{disc}}$), it is important to have an accurate description of their sizes. The disc size will depend on the virial radius of the halo where the galaxy was born, and on its angular momentum. If the halo is asymmetric and surrounded by a clumpy distribution of matter, then it can acquire an angular momentum from a net tidal torque. To quantify the angular momentum of the system, one often refers to the spin parameter, which is a dimensionless quantity, defined as

$$\lambda = \frac{J|E|^{1/2}}{GM_{\text{halo}}^{5/2}}, \quad (12)$$

where J , E , and M_{halo} are the total angular momentum, gravitational binding energy, and mass of the halo. The distribution of the spin parameter as found in N -body simulations (Warren et al. 1992; Cole & Lacey 1996) can be approximated by a log-normal distribution with $\langle \lambda \rangle = 0.05$ and $\sigma_{\lambda} = 0.5$. Hereafter we assume the mean value for λ . Mo et al. (1998) related the disc radius to both the spin parameter and the virial radius by assuming that the angular momentum of the disc is a fixed fraction of that of the halo

$$r_{\text{disc}} = \frac{1}{\sqrt{2}} \left(\frac{j_{\text{d}}}{m_{\text{d}}} \right) \lambda R_{\text{vir}}, \quad (13)$$

where m_{d} is the ratio of the disc mass to the halo mass, and j_{d} is the ratio of the angular momentum of the disc to that of the halo. Higher values of the spin parameter result in larger discs, because they contract less before reaching the centrifugal equilibrium. The above relation holds in the case of halos approximated with isothermal profile and neglecting the gravitational effects of the discs themselves, but the authors also give the correct expression in the case of NFW profiles and self-gravitating discs. As shown by Mo et al. (1998), it is reasonable to assume that $j_{\text{d}} \approx m_{\text{d}}$, which gives us

$$r_{\text{disc}} = \frac{\lambda}{\sqrt{2}} R_{\text{vir}}, \quad (14)$$

leading to galactic discs that are over an order of magnitude less extended than their halo hosts. Based on the assumption that the self-gravity of the disc is negligible, the disc circular velocity is equal to the halo virial velocity.

The assumption that the specific angular momentum of the disc is the same as that of the halo, as implied by $j_{\text{d}} \approx m_{\text{d}}$, leads to disc sizes that closely match those of observed spirals (Mo et al. 1998), hence it became a standard assumption of disc modelling. Nevertheless, hydrodynamical simulations find that the gas loses most of its angular momentum during accretion, producing discs smaller than that observed (Navarro & White 1994). It remains unclear whether this effect is simply due to the limited mass resolution employed, or to the absence of some form of feedback.

3.4. Star formation

The physical processes governing the rate at which the (primordial) gas is transformed into stars play a critical role in models of galaxy formation. Unfortunately, they remain affected by major uncertainties, given the extremely complex interplay of phenomena on the largest (magnetic fields, gas angular momentum), as well as the smallest (radiative cooling, thermal conduction, dust extinction) scales. Nevertheless, observations indicate that some useful laws exist to describe SF on global scales, larger than star-cluster scales. Analysing a large sample of spirals and starburst galaxies, Kennicutt (1998) found two empirical correlations for the star formation per unit area, Σ_{SFR} : (i) $\Sigma_{\text{SFR}} \propto \Sigma_{\text{gas}}^{1.4}$, and (ii) $\Sigma_{\text{SFR}} \propto \Sigma_{\text{gas}}/t_{\text{dyn}}$. These empirical estimates justify the use of parametric forms for the star-formation prescription in semi-analytical models, where the star formation timescale is given by the dynamical time.

In our model we consider two modes of star formation. In the first one, the *quiescent mode*, the star formation rate is simply assumed to be proportional to the amount of cold gas available and inversely proportional to the timescale of star formation, which is assumed here to be the dynamical time of the disc $t_{\text{dyn}} = r_{\text{disc}}/v_{\text{disc}}$. The efficiency of the star formation process is quantified by the free parameter α_{quie} defined by the relation

$$\dot{M}_{*} = \alpha_{\text{quie}} \frac{M_{\text{cool}}}{t_{\text{dyn}}}. \quad (15)$$

Since this gas is assumed to share the same high value of the angular momentum as previously discussed, stars formed in this way are added to the disc component of the galaxy.

The second mode of star formation considered in GECO is the *burst mode*. Starbursts are allowed to occur after a merger between galaxies, which can be caused by the cannibalism of a satellite galaxy by the central one, or a collision between satellites. A strong correlation between galaxy interactions and starburst activity is indeed observed both in the present-day universe and at high redshift. This is for example the case for the Ultra-Luminous Infrared Galaxies (ULIRGs), discovered locally by IRAS and found in large numbers at high- z by ISO and Spitzer, exhibiting the most violent episodes of star formation (Kennicutt 1998; Sanders & Mirabel 1996). The assumption of a starburst triggered by a galaxy merger is furthermore justified by several numerical simulations (Mihos & Hernquist 1994, 1996), which demonstrate how, during the merger phase, gas sinks to the central region of the galaxy and the higher density leads to an enhanced level of star formation (according to the Kennicutt law). Simulations by Cox et al. (2008) indicate that the starburst event can be triggered in major, as well as in minor, mergers, but with an efficiency that depends strongly on the galaxy mass ratio (as implemented also in Somerville et al. 2001; Menci et al. 2004). Therefore, in our model, the star formation during the starburst is given by

$$\dot{M}_{*} = f_{\text{burst}} \frac{M_{\text{cold}}}{t_{\text{burst}}}, \quad (16)$$

where t_{burst} is the dynamical time of the largest disc, while f_{burst} is the efficiency of the burst, which is assumed to be linearly proportional to the merger mass ratio

$$f_{\text{burst}} = \beta_{\text{burst}} \frac{m_1}{m_2}, \quad (17)$$

where m_1 and m_2 are, respectively, the lowest and the highest mass galaxy, and β_{burst} is a free parameter. Stars formed in this way are added to the bulge component of the galaxy.

In addition to increasing the rate of star formation, major mergers between spirals move stars from circular orbits to random motions, hence producing a remnant that generally resembles an elliptical galaxy. For these reasons, we can safely assume that after that kind of merger, the discs previously present in the colliding systems are transformed into a spheroid. We define a merger to be a major one when $\frac{m_1}{m_2} > 1/3$. Spheroid formation by means of disc instability is not considered in the present work.

3.5. Feedback processes

Feedback processes are mechanisms that regulate the efficiency of star formation. The need for some form of feedback in low-mass halos, which suppresses cold gas accretion, was first recognised by [White & Rees \(1978\)](#), to flatten in some way the faint-end of the luminosity function, which was predicted to be steeper than the observational data available at the time. SN feedback and photoionization are commonly considered to reduce the faint-end slope.

Although initially the motivation for invoking feedback was to suppress cooling, and thus star formation, in low-mass halos, the focus has since shifted to attempting to reproduce the bright-end of the luminosity function, which in the most classical models exhibited an excess of bright objects at low redshift compared to the observations. This illustrates the basic problem of transforming the essentially power-law form of the DM mass function into the Schechter exponential function measured for the baryons. Although the behaviour of the cooling function implies that the cooling time is relatively long in high-mass halos, this is insufficient to explain the sudden truncation observed in both the galaxy luminosity and stellar mass functions and some mechanisms preventing the cooling rate in high-mass halos is also needed, which is commonly referred to as the AGN effect (see below).

3.5.1. SN feedback

The first form of feedback considered in our model is that from SN explosions and high-mass stars outflows, which eject gas and energy into the surrounding interstellar medium (ISM). This is supported by several detections of supernova-driven winds in dwarf star-forming galaxies ([Martin 1999](#); [Strickland et al. 2000](#); [Heckman 2001](#)), which implies that the gas reheating rate is proportional to the SFR.

The parametrisation of the SN feedback is based on simple energy arguments. The rate of reheating is assumed to be proportional to the SFR, to the number of supernovae per solar mass of stars, given by $\eta_{\text{SN}} = 4 \times 10^{-3} M_{\odot}$ for a Salpeter initial mass function (IMF), to the energy released by each SN of about $E_{\text{SN}} = 10^{51}$ erg, and to the efficiency with which the SN energy is transferred into the ISM, ϵ_{SN} . This last parameter is highly uncertain, and is usually treated as a free parameter. The rate of reheating is more efficient for galaxies living in low potential wells. To indicate the depths of the potential well of the host halo, we use the halo circular velocity, so that the rate of reheating will be simply proportional to V_c^{-2} . This implies that galaxies living in low-mass halos are affected by SN feedback effects, and that their star formation is self-regulated, while in high-mass halos this kind of feedback is ineffective. The rate of reheating is finally given by

$$\dot{M}_{\text{heat}} = \epsilon_{\text{SN}} \frac{4 \eta_{\text{SN}} E_{\text{SN}} \dot{M}_*}{5 V_c^2} \quad (18)$$

([Kauffmann et al. 1993](#); [Somerville & Primack 1999](#)).

The reheated gas is removed from the cold gas reservoir, and cannot be used to form any new stars. We assume an *ejection* model of feedback, in which the reheated gas is ejected from the halo and is unable to cool until it is reincorporated into a more massive halo at a subsequent step of the merging hierarchy. Although our reincorporation scheme assumes a rapid fall-back of gas (analogous to the fast reincorporation of [De Lucia et al. 2004](#)), we found that it produces superior results to the *retention* model, in which the gas can subsequently cool. In particular, we obtain a closer match to the faint-end of the stellar mass function.

3.5.2. Reionization

It is now known that the hydrogen in the intergalactic medium (IGM) that became neutral at $z \sim 1000$ must have been ionized again at later epochs, although the redshift at which this reionization occurred remains uncertain, ranging from $z = 6$, as imposed by the lack of a Gunn-Peterson trough in quasar spectra at that redshift ([Fan et al. 2000](#)), to $z = 11$, as imposed by the constraint on the optical depth to the last scattering surface measured from WMAP5 data.

If a large population of galaxies and quasars were exist at very high redshift, as predicted by galaxy formation models and confirmed up to $z \sim 6$ by observations ([Fan et al. 2000](#)), then reionization may have occurred by means of photoionization, since both young galaxies and quasars emit UV photons that are able to ionize the IGM. This photoionizing background may also inhibit galaxy formation in two ways. It may heat the IGM, increasing the thermal pressure of the gas and preventing its collapse into the dark matter halos, or the cooling rate may be reduced decreasing the number of neutral atoms that may be collisionally excited and causing a strong suppression of galaxy formation in low-mass halos.

According to previous studies ([Thoul & Weinberg 1996](#); [Gnedin 2000](#); [Somerville 2002](#)), after reionization the above mechanisms prevent gas accretion in halos with $V_c < 50 \text{ km s}^{-1}$, with the result that galaxy formation is strongly suppressed in these systems. Hence, in our model, we mimic the effect of photoionization by suppressing gas cooling in halos with a circular velocity lower than that at redshifts greater than the redshift of reionization, assumed to be $z_{\text{re}} = 6$. Although the precise value of the redshift at which reionization begins remain uncertain and other models treat it as a free parameter, we found that by varying its value our results do not change appreciably and we therefore choose to keep it fixed. This agrees with previous works that found that the properties of the galaxy population are almost insensitive to the assumed redshift of reionization ([Kravtsov et al. 2004](#); [Macciò et al. 2010](#)). At very high redshift, the “leaves of the tree” are of very low mass and the only cooling mechanism is the H_2 cooling, which is very inefficient.

The simple approach used in our model for the reionization was demonstrated by [Benson et al. \(2003\)](#) to have very similar effects on the self-consistent treatment of the photoionization described, for instance, in [Benson et al. \(2002\)](#). In Appendix B, we present the effect of varying the assumption about the limit of the circular velocity.

3.5.3. AGN feedback

There is growing evidence of a tight relationship between galaxy evolution and the growth of supermassive black holes (SMBHs) powering nuclear activity. Strong evidence is given by the tight correlations between the BH mass and the mass of the bulge

(Häring & Rix 2004), and that between the black hole mass and the velocity dispersion of stars in the bulge (Ferrarese & Merritt 2000; Gebhardt et al. 2000). The mutual feedback between galaxies and quasars may be the origin of these strong correlations.

We implement the accretion onto black holes in our model following the prescriptions of Kauffmann & Haehnelt (2000) and Croton et al. (2006). We allow two different modes of feedback, one following the starburst triggered by galaxy mergers and strong interactions, the *quasar mode*, and a second one, the *radio mode*, taking place at a low rate during the whole life of the galaxy. A third natural means of growth for SMBHs is the coalescence of the BHs residing at the centre of two merging galaxies. In this case, after the merger of the host galaxies, the new BH mass is simply the sum of the two progenitors. We thus simplify our treatment by ignoring the occurrence of BH binary systems and gravitational wave losses of angular momentum.

As a starting point we use a seed mass for the BH in the galaxies at the bottom of hierarchy, i.e. living in the “leaf” halos. These seeds are believed to form at very high redshift, but it is quite unclear if they formed from the direct collapse of pre-galactic gaseous discs or if they are the remnants of massive Population III stars (Volonteri et al. 2008). We considered a seed mass equal to $1000 M_{\odot}$, and checked the consequence of this choice by using different mass values, finding that our results do not depend on this choice, at least for low seed masses. Since we began by placing the seeds at the bottom of the hierarchy, the redshift at which they are planted depends upon the time at which the leaf halo mass falls below the mass resolution of the tree, which can be higher than the redshift of the reionization. In all cases, they cannot grow before the reionization starts since gas accretion, which is the main mechanism of feeding BHs, is inhibited.

The first mode of accretion is motivated by the observations of bright AGN and quasars radiating with high efficiency, close to their Eddington limit. It is widely believed that this mechanism of accretion is triggered by galaxy mergers, since they can drive rapid inflows of gas toward the centre of the galaxy, feeding both the starburst and the BH.

As in Kauffmann & Haehnelt (2000), we assume that during a merger of galaxies a certain fraction of cold gas is accreted onto the centre of the black hole

$$\dot{M}_{\text{BH}}^{\text{QSO}} = \frac{f_{\text{BH}} M_{\text{cold}}}{1 + (280 \text{ km s}^{-1}/V_c)^2} \Delta\tau^{-1}, \quad (19)$$

where f_{BH} is an efficiency parameter to be chosen to match the relation between black-hole mass and velocity dispersion of the bulges, and $\Delta\tau$ is the time interval of the integration of differential equations. In this way, QSO accretion is closely linked to the starburst activity of the galaxy, which is triggered both by galaxy mergers and BH accretion, naturally producing BH masses proportional to the mass of the spheroidal component formed only during the starburst.

The second means of accreting gas, the radio mode, is a continuous and quiescent accretion that occurs throughout the lifetime of the galaxy, during which the black-hole accretes gas directly from the hot halo. This is supported by observations of radio galaxies (mainly in high-density environments, such as groups or clusters of galaxies), which accrete at a sub-Eddington rate, hence in a rather inefficient fashion. In spite of this inefficiency, the energy extracted from the BH accretion in the form of collimated jets is believed to contrast the cooling flow at the centre of clusters. Assuming that in this case the BH is fuelled

with a Bondi accretion rate, the resulting BH growth rate is given by (Croton et al. 2006; Somerville et al. 2008)

$$\dot{M}_{\text{BH}}^{\text{RADIO}} = k_{\text{AGN}} \frac{M_{\text{BH}}}{10^8 M_{\odot}} \frac{f_{\text{hot}}}{0.1} \left(\frac{V_c}{200 \text{ km s}^{-1}} \right)^3, \quad (20)$$

where f_{hot} is the ratio of the hot gas mass to the halo mass, and k_{AGN} is a free parameter with the dimensions of an accretion rate ($M_{\odot} \text{ yr}^{-1}$).

The most important means of increasing the mass of the black hole is the *quasar mode*, in which the accretion rate can be much greater than that given by the Eddington luminosity. The second accretion mode, the *radio mode*, provides a negligible contribution to the present-day black-hole masses, being several orders of magnitude below the Eddington rate. Nevertheless, this is an important source of feedback in high mass halos, because it suppresses cooling flows as well as the quasar mode mechanism, and it occurs throughout the galaxy lifetime, while the *quasar mode* acts only during a very short period of the galaxy life. The feedback efficiencies of these processes, which are very difficult to model a-priori, are determined by trying to match various observables. The efficiency of the *quasar mode* accretion is defined by attempting to reproduce the $M_{\text{BH}} - M_{\text{bulge}}$ relation, while the *radio mode* accretion efficiency is constrained by optimizing the shape of the stellar mass function, and in particular the observed knee at the characteristic stellar mass.

The injection of energy into the ISM by an AGN is modelled in the following way. The mechanical heating generated by the black hole accretion is given by

$$L_{\text{BH}} = \eta \dot{M}_{\text{BH}} c^2, \quad (21)$$

where c is the speed of light and η is the global efficiency of energy production close to the event horizon in nuclear black-holes, and is set to the reference value of 0.1. The gas cooling rate in the halo is then corrected by this energy injection according to

$$\dot{M}_{\text{cool}}^{\text{new}} = \dot{M}_{\text{cool}}^{\text{old}} - \frac{L_{\text{BH}}}{V_c^2/2}. \quad (22)$$

To avoid an unphysical negative value for the cold gas accretion rate, we impose mass conservation by assuming an amount of newly formed cold gas mass in the time-step $\Delta\tau$ the maximum between zero and $\dot{M}_{\text{cool}}^{\text{new}} \Delta\tau$, where $\dot{M}_{\text{cool}}^{\text{new}}$ is given by Eq. (22). Hence, the cooling rate may not only be reduced, but even stopped in the case of a strong BH accretion rate.

3.6. Galaxy dynamics

During the merger of two dark matter halos, the baryonic cores that they contain, being more compact and less subject to tidal effects, may avoid merging with each other, and end up orbiting within the new combined halo. A halo formed by many mergers may contain many distinct galaxies, with the galaxy in the most massive halo becoming the central galaxy and all the others becoming the satellites. These satellite galaxies gradually lose their energy and angular momentum under the action of dynamical friction until they sink to the centre of the halo and merge with the central galaxy. Moreover, they are subject to random gravitational collisions that can occur with other satellites.

3.6.1. Dynamical friction

The effect of dynamical friction in slowing down the orbital velocities of galaxies moving through a sea of dark matter particles

was originally described by Chandrasekhar (1943) and previous SAMs have adopted this approach. Although early N -body studies (Navarro et al. 1995) supported the merger timescales predicted by the classical approach, numerical and hydrodynamical simulations (Jiang et al. 2008; Boylan-Kolchin et al. 2008) have shown that the Chandrasekhar’s approach underestimates the merger timescale for minor mergers and overestimates it for major merger events. As an estimate of the dynamical friction timescale, we assumed the fitting formula of Jiang et al. (2008), derived from hydro/ N -body simulations:

$$t_{\text{df}} = \frac{0.94\epsilon^{0.6} + 0.6}{2C} \frac{M_{\text{halo}}}{m} \frac{1}{\ln(\Lambda)} \frac{R_{\text{vir}}}{V_c}, \quad (23)$$

where C is a constant equal to 0.43, $\ln \Lambda$ is the Coulomb logarithm, which can be approximated to be $\ln \Lambda = \ln(1 + M_{\text{halo}}/m)$, ϵ is the circularity parameter of the satellite’s orbit, given by $\epsilon = J/J_c$, where J is the angular momentum of the actual orbit and J_c that of the circular orbit with the same energy. We adopt the average value found in numerical simulations of $\langle \epsilon \rangle = 0.51$ (Tormen 1997; Jiang et al. 2008).

We note that the timescale increases as the halo mass increases, so that at high redshift, when the halos are less massive, we find a high rate of merging, which is lower at low redshift, where we observe an accumulation of sub-halos inside the parent halo.

An important consideration concerns the mass m used to compute the dynamical friction time-scale. As soon as a galaxy becomes a satellite in a larger halo, its initial mass is determined by its total (dark matter and baryonic) mass. However, as it moves towards the centre of the larger halo, a large fraction of its dark halo is stripped away, while the mass of the gaseous core is too dense to be stripped. Thus, the effective mass of the satellite decreases with time and the dynamical friction timescale should increase. When neglecting this effect, we found that the timescales for merging were too small, leading to overmerging, particularly at low redshifts. We have taken into account the effect of tidal stripping by allowing the mass of satellite to vary with time according to the timescales predicted by Taffoni et al. (2003). We therefore assume that the satellite loses its dark halo 1.5–2 Gyr after entering the virial radius (for simplicity here we neglect the tidal stripping on the baryonic core, hence do not consider tidally destroyed satellites).

3.6.2. Satellite collisions

In addition to the mergers driven by dynamical friction, we include random collisions between satellites. We consider for the satellite encounters the merger rate of Mamon (1992), which is found by integrating over the merger cross-section of Roos & Norman (1979)

$$k = 2 \sqrt{\pi} \alpha_p^2 \alpha_v R_{\text{vir}}^2 v_{\text{gal}} K(V_c/v_{\text{gal}}), \quad (24)$$

where v_{gal} is the internal velocity dispersion of the satellite galaxy, V_c and R_{vir} are the circular velocity and virial radius of the host halo, respectively, $\alpha_p = 4$ and $\alpha_v = 5.4$ are dimensionless parameters, and K is a dimensionless merger rate given by

$$K = \left[\frac{1}{x} + \frac{2}{x^3} - \frac{2 \exp(-x^2)}{x^3} - \frac{3 \sqrt{\pi} \operatorname{erf}(x)}{2 x^2} \right] \quad (25)$$

$$x = \frac{\alpha_v v_{\text{gal}}}{2V_c}. \quad (26)$$

For realistic values of the ratio V_c/v_{gal} , the merger rate decreases with this ratio and becomes very low for galaxy clusters. Given the merger rate, we can compute the collision time to be

$$t_{\text{coll}} = \frac{1}{kn}, \quad (27)$$

where n is the number densities of galaxies in the halo. We obtain a shorter merger timescale at high redshift, when the number density of galaxies is higher. The probability of having a merger between a given satellite and another one, randomly chosen, will be $P = \Delta t/t_{\text{coll}}$, where Δt is the lifetime of the halo. We consider only binary mergers, and we assume that this event occurs when $P \geq 1$. During a collision between two satellites, we allow a burst of star formation in the same way as the one occurring during a merger between a satellite and the central galaxy. The effect of including this process, in addition to the mergers involving the central galaxy caused by dynamical friction, is to decrease the fraction of low-mass galaxies in favour of intermediate-high mass objects, hence to slightly modify the shape of the galaxy mass function.

3.6.3. Remnant

After the merger, the total mass of the remnant (dark matter and baryons) is the sum of the two merging galaxies, while the new radius and circular velocities are computed by applying the conservation of energy and the virial theorem. According to the virial theorem, the total internal energy is given by $E_{\text{int}} = -T$. By applying the conservation of energy

$$T_{\text{new}} = T_1 + T_2 - E_{\text{orb}}, \quad (28)$$

where T denotes the kinetic energy and E_{orb} is the mutual orbital energy

$$E_{\text{orb}} = -f_{\text{orb}} \frac{Gm_1m_2}{r_1 + r_2} \quad (29)$$

(r_1 and r_2 are the radius of the two progenitors and f_{orb} is a parameter that weakly depends on the density profile, we assume that $f_{\text{orb}} = 2$). These considerations yield

$$R_{\text{new}} = \frac{(m_1 + m_2)^2}{m_1^2/r_1 + m_2^2/r_2 + f_{\text{orb}}m_1m_2/(r_1 + r_2)}. \quad (30)$$

In the case of major mergers involving two equal galaxies ($m_1 = m_2$ and $r_1 = r_2$), the size of the remnant is a factor of 4/3 greater than the initial size.

3.7. Galaxy morphology

In our model, the morphology of a galaxy is determined by the relative importance of the bulge over the disc component. The only way of forming discs is by means of the quiescent mode of star formation. In contrast, bulges can grow in two ways: (1) by means of star formation occurring in a starburst event, hence triggered by any merger event; and (2) by means of the disruption of discs following a major merger. In this case, all the stars belonging to the discs undergoing a merger are added to the bulge of the remnant galaxy. This galaxy may eventually form a new disc if a fraction of its cold gas is still present.

We can assign a crude morphological type to each galaxy by using the ratio of the bulge mass to the total stellar mass: $r = M_{\text{bulge}}/M_{\text{star}}$. Using the prescription of Bertone et al. (2007), we classify as ellipticals, galaxies with more than 70% of their stars in the bulge, as spirals, galaxies with $0 < r \leq 0.7$, and as irregulars, galaxies without any bulge.

Table 1. Free parameters.

Parameter	Meaning	Best-fit value	Range
α_{quie}	star formation	0.01	0.01–0.1
β_{burst}	burst efficiency	0.68	0.5–1
ϵ_{SN}	SN feedback efficiency	0.5	0.01–1
f_{BH}	AGN feedback efficiency in QSO mode	0.006	0.001–0.1
k_{AGN}	AGN feedback efficiency in radio mode	1×10^{-6}	10^{-7} – 10^{-6}

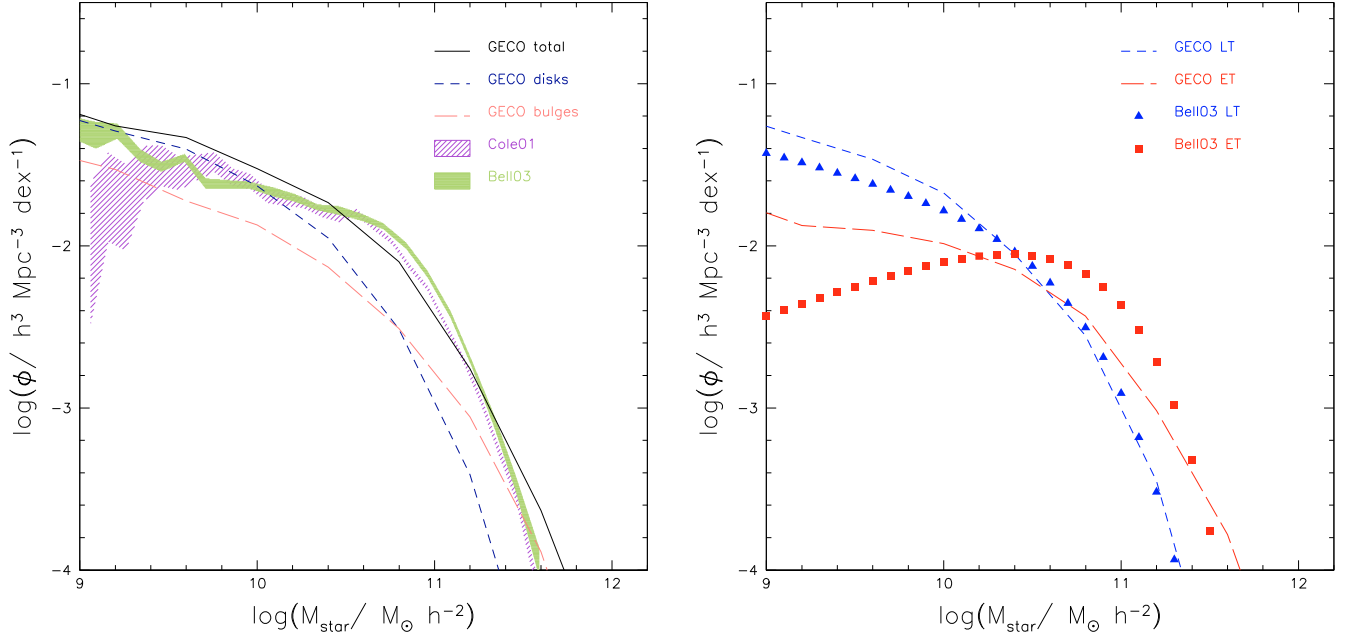


Fig. 2. *Left panel:* stellar mass function at $z = 0$. Black solid line represents the SMF resulting from GECCO, purple shaded region stays for the C01 observed mass function with its error-bar, and the green shaded one from B03. Also shown is the contribution to the total stellar mass content from bulges (red long dashed line) and discs (blue short dashed line). *Right panel:* stellar mass function at $z = 0$ of early-type (red long dashed line) and late-type galaxies (blue short dashed line) compared with the observed one by B03: red squares for early-type and blue triangles for late-type.

4. Setting the free parameters

In the previous section, we introduced several free parameters into the analytical prescriptions modelling galaxy formation. In summary, they are:

1. α_{quie} : efficiency of star formation in quiescent mode;
2. β_{burst} : efficiency of star formation in starbursts;
3. ϵ_{SN} : efficiency of SN feedback;
4. f_{BH} : efficiency of AGN feedback in the *quasar* mode;
5. k_{AGN} : efficiency of AGN feedback in the *radio* mode.

We first infer constraints on their values by comparing the model results, obtained for a large grid of parameter values, with observations of the local universe. In particular, we focus on the build-up of the stellar mass, and we attempt to ensure that our model reproduces the local stellar mass function, as well as the relationship between the black-hole mass and the bulge mass. The stellar mass function is obviously influenced by all the parameters together. The star formation efficiency in the quiescent mode α_{quie} affects the overall shape and normalisation of the function: ϵ_{SN} affects the faint-end (or low-mass end), and β_{burst} determines the contribution of the bulge to the total stellar content, and we ensure that at the bright end, bulges dominate over discs. The AGN efficiencies, f_{BH} and k_{AGN} , shape the bright end of the mass function. The AGN efficiency in the *quasar* mode, i.e., the one triggered by the starburst episode, determines the relationship between the mass of the black-hole and the bulge

mass, affecting mainly the normalisation of the relation, while the slope of the relation is found to be very close to that observed almost independently of the value of this efficiency, since in the model the growth of BHs and bulges are closely linked. In Table 1, we report the value of these parameters in our best-fit model and the allowed range. Unless otherwise stated, in the following we always refer to this best-fit model.

5. Matching data from the local universe

A key observable for comparing predictions of any models of galaxy formation is the number density of galaxies as a function of their stellar mass in the local universe, the stellar mass function (SMF) at $z = 0$. We use it to constrain our model free parameters. We refer to two measurements of the local SMF. The first is that reported by Cole et al. (2001), hereafter C01, obtained by combining data from the Two Micron All Sky Survey (2MASS) and the 2dF Galaxy Redshift Survey. The second estimate, by Bell et al. (2003), exploited a large sample from 2MASS and the Sloan Digital Sky Survey (SDSS). We choose to show their *g*-selected sample (taken from their Table 5). Both estimates use near-infrared data to compute stellar masses and hence are highly reliable. All data are transformed to a Salpeter IMF.

In the left panel of Fig. 2 we show the stellar mass function at $z = 0$, resulting from the model and compared with the C01 and B03 observations. The model is able to reproduce with

good accuracy the shape and normalisation of the SMF, especially at the bright end ($M_{\text{star}} > 10^{11} M_{\odot} h^{-1}$). Compared to the C01 mass function, the model shows a slight excess of galaxies at the faint-end. However, the B03 estimate has a steeper faint end, resulting in closer agreement with our prediction. Our model also underestimates galaxies at the knee of the mass function ($10^{10.5} - 10^{11} M_{\odot}/h^2$), an effect already present, for instance, in the Millennium galaxy catalogue (Bertone et al. 2007). This dearth may be partly explained as the combined effect of SN and AGN feedback that are both effective in this mass range. Moreover, since the deficit is due to a lack of intermediate-mass early-type galaxies (see right panel of Fig. 2) it is probably connected to the excess of low-mass spheroids, because satellite galaxies are unable to become massive enough in the model for the reasons described later in this section.

We highlight the fundamentally different shapes of the halo mass and the luminous (stellar) mass functions presented here. The general shape of the dark matter halo mass function (see Fig. 1), as predicted by any theoretical model based on hierarchical dark-matter clustering, is a pure power-law with a steep faint-end and no knee at high masses. A turn-off mass does exist, but occurs at much higher masses ($M \sim 10^{15} M_{\odot}$) than the characteristic one observed in the stellar mass function. To obtain a Schechter shape for the mass function, many effects contribute. At the faint-end side, the feedback from both SN and the photoionization background suppresses star formation in small halos, hence reducing the faint-end slope. At the bright-end, the difference between the exponential cut-off observed in the stellar mass function and the power-law shape expected for the halo mass function is explained by the interplay between various independent effects. On the one hand, there is a marked dependence of the gas cooling on the halo mass: the cooling time decreases with halo mass. In addition, the two modes of gas cooling discussed in Sect. 4.3 have a halo mass dependence: in the *cold mode* regime, the gas accretes towards the centre in a time-scale given by the free-fall time, while in the *hot mode* regime the accretion rate is governed by the cooling time, and is much less efficient than in the former case. Since in high-mass halos, the accretion occurs mainly by means of this last mechanism, this may explain why in these halos gas is unable to cool efficiently. Moreover, the AGN feedback acting on this scales, reduces the cooling rate, leading to an approximately correct number of massive galaxies.

In Fig. 2 (left panel), the separate contributions to the total stellar content from discs and bulges are also shown, as blue short-dashed and red long-dashed lines, respectively. As expected, the bright-end is dominated by bulges, meaning that objects of very high-mass ($M_{\text{star}} > 10^{11} M_{\odot} h^{-1}$) essentially do not contain discs, which have presumably been destroyed during a major merger. In contrast, discs overcome the number densities of bulges at low masses, and start to be dominant in the mass range $M_{\text{star}} \sim 10^{10.5} M_{\odot} h^{-1}$. We note that this value is close to the transition mass, $\sim 3 \times 10^{10} M_{\odot} h^{-1}$ at $z = 0$, at which a transition in several galaxy properties is observed (Kauffmann et al. 2003) and where early-type galaxies begin to dominate over the late-type ones in the local universe (Baldry et al. 2004; Bundy et al. 2005).

We have so far considered only the contribution to the total stellar mass density from the disc and bulge components. In the right-end panel of Fig. 2, we show the mass functions of both early-type and late-type galaxies. As defined in the previous section, early-type galaxies are defined as galaxies whose bulge represents at least 70% of the total stellar mass. In the definition of late-type systems, we include both spiral and irregular galaxies.

We compare the predicted mass function with the results of B03. With this definition of morphologies, the agreement with the observational data is quite good; in particular, we accurately reproduce the transition mass at which the number density of ellipticals/S0s equals that of late-type galaxies locally. However, we note quite a large excess of faint early-type galaxies with masses below $10^{10} M_{\odot}/h^2$. This is a long-standing problem that afflicts many SAMs in the literature (Weinmann et al. 2006; Croton et al. 2006; Cattaneo et al. 2008; Somerville et al. 2008) and may be regarded as an indication of an incorrect treatment of the satellite population. A common way among SAMs of treating the satellites is to assume that the hot gas in a system that merges into a more massive one is instantaneously stripped (strangulated) and added to the reservoir of the new central galaxy. As a consequence, the star formation in the new satellite is quenched shortly after it has consumed its cold gas. This crude treatment of strangulation is clearly an oversimplification, and hydrodynamical simulations indicate that this process occurs on a longer timescale, of the order of 1–10 Gyr (McCarthy et al. 2008), allowing the star formation to continue for some time after the coalescence, hence lowering the fraction of red satellites (Kang & van den Bosch 2008). Although even tidal disruption (see for instance Somerville et al. 2008) can help in decreasing the faint-end, it is unlikely that it can change the relative numbers of early and late-type satellites (Kimm et al. 2009). Other effects, such as those of ram pressure on the cold gas in the galaxy (Lanzoni et al. 2005) may also play a role in the formation of the satellite population and should be included in future SAMs.

To determine the efficiency of black-hole growth, we constrain our model to match the observed relation between the black-hole mass and the mass of the stellar bulge in the local universe. Since the major channel of black-hole growth is given by accretion during the *quasar* mode triggered during a starburst event, when all the stars formed are added to the bulge component, it comes as no surprise that black-hole and bulge masses are closely linked. Nevertheless, to obtain an acceptable fit, where both the slope and the normalisation of the relation are well reproduced, some fine tuning of the f_{BH} and k_{AGN} parameters was required.

In Fig. 3, we compare our derived relation (blue triangles) with data from Haring & Rix (2004), represented by the black squares with error-bars, and their best-fit relation, shown by the magenta line. The observed relation is well reproduced by our model over the whole mass range (note in any case that the Haring & Rix (2004) fit is derived only for bulge masses $M_{\text{bulge}} > 10^{10} M_{\odot}$). However, the scatter in the model relation is smaller than that observed, as the model neglects the contribution to the bulge formation caused by disk instabilities, and the only means of forming spheroids is through mergers, hence linked directly to the BH formation.

We present an additional test performed on the black-hole population in Fig. 4, where we compare the BH mass function of the model with the local estimate by Shankar et al. (2004). The remarkable agreement between the observed and predicted BH number densities, and the closely matched BH-bulge relation is encouraging and suggests that our means of implementing AGN feedback, although simple, is accurate enough.

6. Comparing GECO with high-redshift galaxy statistics

Having obtained in the previous section a good match of GECO's predictions with the global properties of galaxies in the

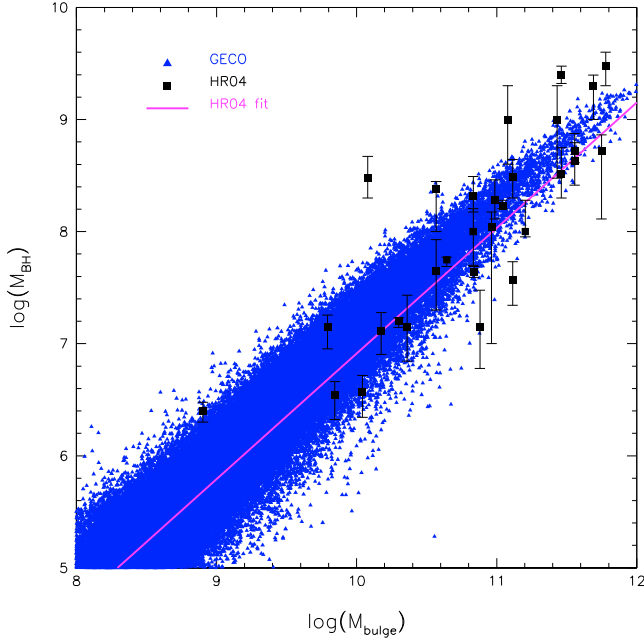


Fig. 3. Black-hole versus bulge mass relation at $z = 0$. Blue triangles represent data for modelled galaxies, while black squares with error bars are data from Häring & Rix (2004). The magenta solid line is their best-fit relation.

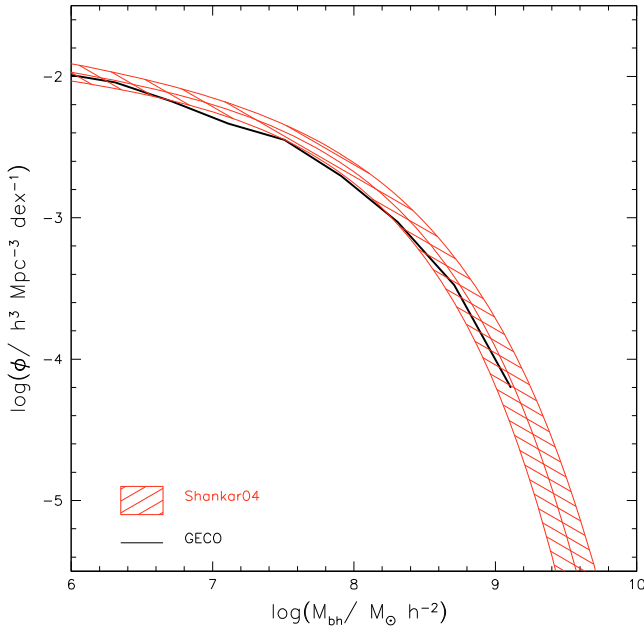


Fig. 4. Local black-hole mass function of the model (black solid line) compared with the estimates of Shankar et al. (2004) (red shaded region).

local universe, it is now instructive to attempt a first comparison of the evolutionary properties of the model with the galaxy statistics in the distant universe, with no further adjustment of the model parameters. Given the wide range of physical processes included in GECO, one would expect at least rough agreement with the global properties, unless some key physical processes have been overlooked.

6.1. The evolution of the stellar mass function

We first compare our predicted mass function with observations up to $z \sim 3.5$. In Fig. 5 we compare GECO's mass functions with those observed by Franceschini et al. (2006), hereafter FR06, Fontana et al. (2006), hereafter F06, Pérez-González et al. (2008), PG08, Marchesini et al. (2009), M08 and Berta et al. (2007), B07. All data have been transformed to a Salpeter IMF. We consider only mass function estimates that take into account IRAC bands in the stellar mass derivation, since the lack of Spitzer data in the near-IR leads to an overestimate of the stellar masses at $z > 3$ (see F06). We note that error-bars in FR06 only take into account Poisson statistics, hence are much smaller than in the other data, where uncertainties in photometric redshifts, stellar masses, and cosmic variance are considered.

Considering the spread between different estimates of the mass function, the comoving number density of massive galaxies in our model is roughly consistent with the observed values, although with a tendency to underpredict the data, especially at high redshifts. In the highest redshift bin considered ($z \sim 3.5$), the bright-end is marginally consistent with that of F06 but systematically lower than M08 and PG07. We note, however, that including the effects of different assumptions about the spectral energy distribution (SED) modelling produces slightly different MF estimates, that are fully consistent with each other (see M08).

In the comparison of model expectations with the data, a remarkable feature concerns the faint end of the mass function, where the model tends to keep systematically in excess of the observed number of low-mass objects at all redshifts. There is significant evolution in the number density of low mass galaxies in the data, whereas the model predicts modest or no evolution up to redshift of one. This disagreement between data and hierarchical models at the faint-end of mass function seems a common feature of various models (Fontana et al. 2006; Fontanot et al. 2009; Monaco et al. 2009).

In the same Fig. 5, we also include the SMF predictions adopting the WMAP5 set of parameters, which are indicated by the red dashed line. The main difference from the Concordance cosmology is a lower value of σ_8 and a tilt in the primordial power spectrum ($n < 1$), which causes a delay in the formation of structures. This delay is observed in the evolution of the SMF, where, at high redshift the model predicts a later assembly of galaxies, exacerbating the underproduction of massive galaxies at higher redshifts.

We note, however, that this comparison must be interpreted with caution before deriving firm conclusions. The errors in the stellar mass estimates can strongly affect (in the sense of increasing) the counts at the bright-end where the mass function is very steep. An improved approach would be to convolve the model stellar mass function with the error distribution in the stellar mass given by the observations (Kitzbichler & White 2006; Stringer et al. 2009; Cattaneo et al. 2008). Of course, the uncertainties in the stellar mass estimates increase with redshift and this can influence the observed evolution of the stellar mass function.

Finally, it is not unlikely that the derivation of the stellar mass function at the faint-end might have been significantly influenced by incompleteness effects in the source selection, which has produced a spurious evolution at low masses. More extensive deep imaging by Spitzer will be carried out on large areas during the warm mission phase, which will offer an opportunity of addressing these issues shortly.

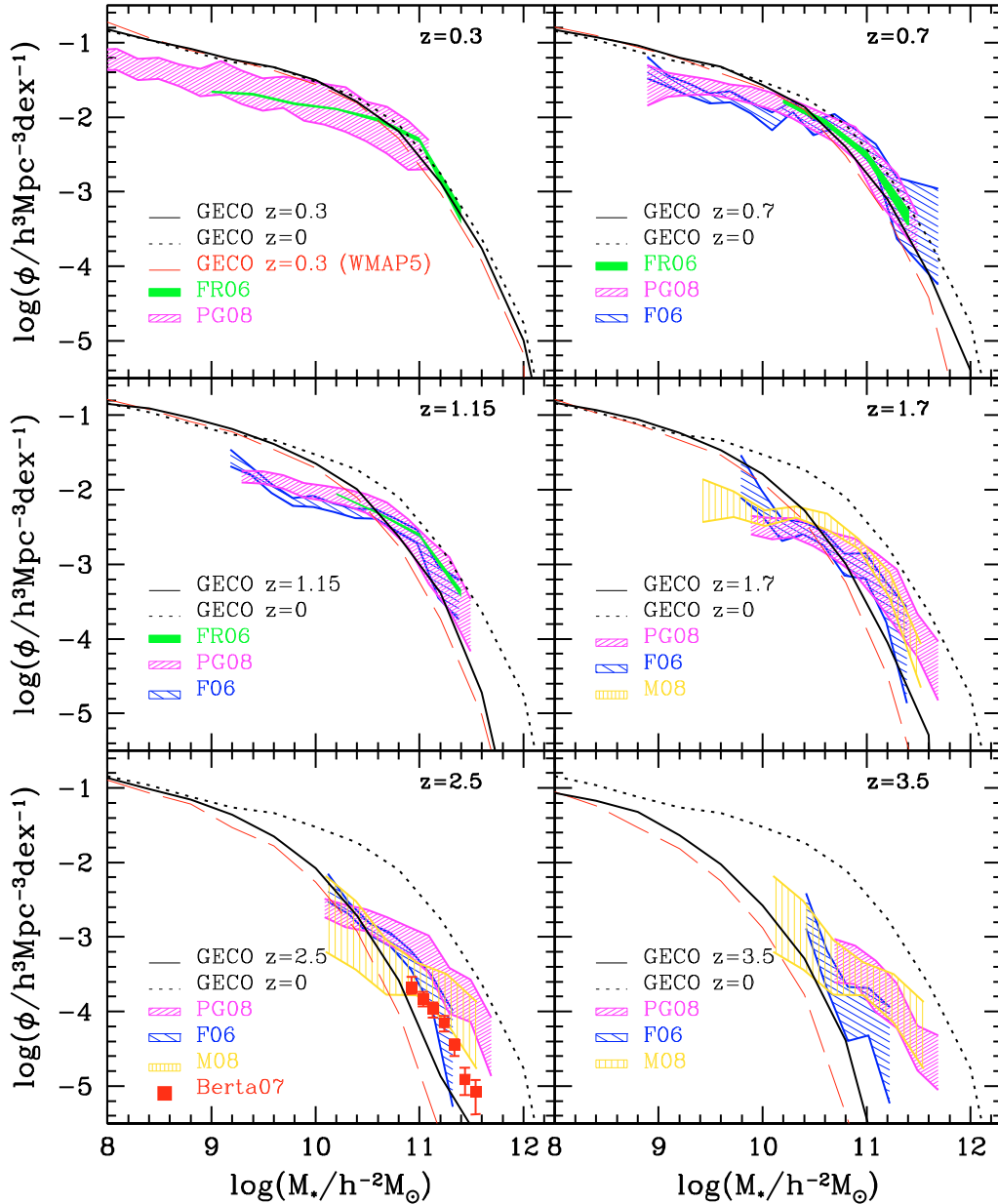


Fig. 5. Comparison between GECO's mass functions at high redshift, up to $z \sim 3.5$. The green shaded region indicates the mass function of Franceschini et al. (2006), the magenta one is that of Pérez-González et al. (2008), the blue region is the estimate of Fontana et al. (2006), the yellow shading is from Marchesini et al. (2009) and the red squares at $z \sim 2$ show the results from Berta et al. (2007). GECO predictions are represented by a solid black line. The dotted line in all the panels is the GECO mass function at $z = 0$, reported as reference and the red dashed line is the model prediction for the WMAP5 cosmology.

6.2. Quasar luminosity function

The gas accretion onto black holes described in Sect. 3.5.3 triggers the AGN activity whose associated bolometric luminosity is given by L_{BH} (Eq. (21)). Although the accretion rate in our model is not limited by the Eddington rate, we constrain the quasar luminosity to be below this limit

$$L_{\text{QSO}} = \max(L_{\text{BH}}, L_{\text{Edd}}). \quad (31)$$

To test the accuracy of our modelled feedback from AGN activity on the galaxy population, we compare the quasar luminosity function predicted by GECO with observational estimates. To avoid introducing additional uncertainties caused by the obscuration factor in the optical bands, we compare our predictions with bolometric luminosity functions. We refer to the

compilation from Hopkins et al. (2007a), obtained by collecting a large multiwavelength dataset, from the optical, soft and hard X-ray, near- and mid-IR. The authors give obscuration-corrected luminosities, aimed to represent the intrinsic quasar population. In Fig. 6, we show our predicted quasar luminosity function up to $z = 2$. The model gives an acceptable description of the evolving quasar population at low and intermediate redshift, but at higher redshift (panel at $z = 2$) it underpredicts the number of luminous quasars. Varying the efficiency of the accretion onto the black hole (f_{BH} and k_{AGN}) does not solve the problem, because the match at high redshift would be obtained at the expense of the agreement with the local black-hole mass function. This may be an indication that the parametrisation of the AGN activity used in the present work is not completely adequate, as already suggested by Marulli et al. (2008), and an

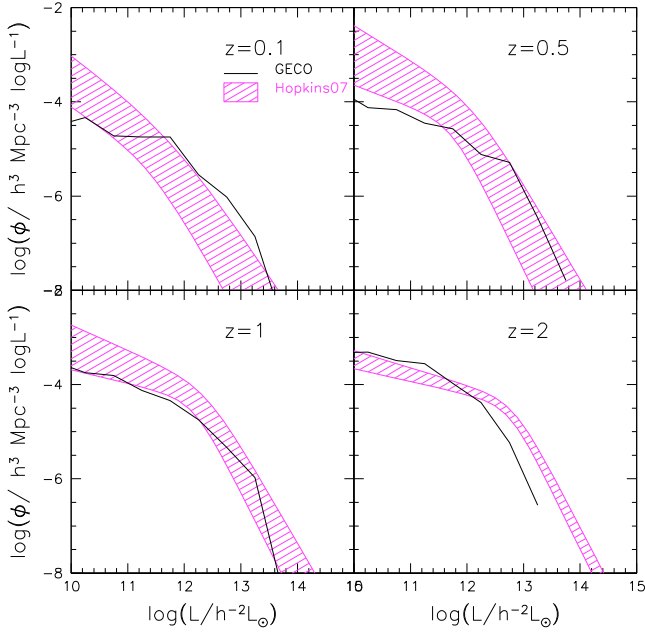


Fig. 6. Comparison between GECO’s quasar luminosity functions at different redshifts and observations by Hopkins et al. (2007a). The magenta shaded region indicates the quasar luminosity function of Hopkins et al. (2007a), while GECO predictions are represented with a solid black line.

accretion efficiency that increases with redshift may be required (as suggested even by hydrodynamical simulations, see Viola et al. 2008), to fit simultaneously the low and the high redshift luminosity functions (Marulli et al. 2008; Lapi et al. 2006). We also suggest that higher accretion efficiencies at high redshift may be achieved with an enhanced cooling efficiency at early times. This alternative may also provide a way of forming galaxies more efficiently at high redshift, hence improving the match with the stellar mass function evolution.

6.3. Formation histories of the stellar populations

To achieve a deeper insight into the process of the stellar mass build-up of our modelled galaxies, we investigate their detailed star formation histories (SFH). We derive the SFH a posteriori for each present-day galaxy, taking into account its baryonic tree and summing up all the stellar populations formed inside its progenitors. We compute the SFHs over 52 time-steps, our predefined grid of times used for the merger tree. We show in Fig. 7, as an example, the SFHs for 4 different realizations of the central galaxy of a halo with mass $5 \times 10^{12} M_{\odot}$, i.e., very similar to the Milky-Way halo. We indicate the stars formed in the quiescent mode with a blue shaded histogram and with a red one the stars formed during the starburst phase. The black envelope is the sum of both contributions. In each panels, the host halo mass and stellar mass are indicated, together with the parameter r , which is the ratio of the bulge to the total stellar mass.

In the case of such a Milky-Way-like halo, the majority of the central galaxies are spirals ($\sim 60\%$). However, the mix of galaxy properties is found to be rather heterogeneous. In the lower-right panel, we see an example of a quite smooth star formation history with a steep rise in SFR at early times followed by a smooth decrease. In the two upper panels, we see that there is more than one peak of quiescent star formation, indicating that star formation has occurred in different progenitors of the final galaxy.

In other cases, the starburst may have occurred at more recent times ($z \lesssim 0.5$ in the lower-left panel) and have been more efficient in consuming all the gas, hence the galaxy has evolved passively until present. In all the cases represented, starburst events are very frequent at early times, even in galaxies that at the present time have a late-type morphology.

To estimate the age of a galaxy, we define its formation redshift as the redshift when the galaxy has formed half of its present-day stellar mass. We indicate this in Fig. 7 as a vertical dashed line. Galaxies that have experienced a smooth, quiescent star formation tend to form their stars later, while galaxies having experienced a more bursty star formation history, thus having an elliptical morphology, tend to have higher formation redshifts.

In Fig. 8, we show the SFH of the central galaxy of halos with different mass, averaged over 100 realizations of the same parent halo tree. Halo masses range from $\sim 10^{11} M_{\odot}$ to $\sim 10^{14} M_{\odot}$. We note that, while in Fig. 7 the SFHs refer to single realizations of one halo, each panel here refers to the average over 100 realizations of the same halo, hence SFHs appear to be smoother. Two trends can be noted with the halo mass. The first is that, passing from low-mass to high-mass halos, the starbursts become the dominant mechanism of star formation. The second is that the star formation rate for galaxies living in high-mass halos reaches a maximum at higher redshift than for those in low-mass halos. Therefore, the associated formation redshift for more massive objects is higher. The increasing importance of the starburst mode with mass, and its related AGN feedback, lead to a rapid consumption of gas at early times, by preventing the gas cooling and inhibiting additional star formation. The consequence is a lower rate of star formation at later times, hence higher average formation redshifts for galaxies living in higher mass halos.

Since high-mass galaxies live in high-mass halos, these results indicate that stars in massive galaxies are on average older than in their less massive counterparts. Nevertheless, even in massive galaxies the star formation is not completely quenched, but a long tail of star formation remains at low redshift. This behaviour of our SFHs appears to be in general agreement with the evidence for a *downsizing* pattern of galaxy evolution, an effect that has been discussed for a long time (Cowie et al. 1996; Gavazzi & Scodreggio 1996; Franceschini et al. 1998; Thomas et al. 2005). We discuss the physical reasons for this in Sect. 7.

6.4. The cosmic star formation rate density

The evolution of the comoving star-formation-rate density for the whole galaxy population is shown in Fig. 9 (left panel). Our model prediction is shown by the black line and is compared with data from the compilation by Hopkins (2004), for UV, optical, and radio tracers, and from Rodighiero et al. (2010) for the IR tracers. Different colours indicate different tracers for the SFR: cyan for star formation derived from the UV continuum, green for optical tracers (OII, H α , and H β), magenta for data using radio tracers and red for SFR estimates derived from the IR luminosity. The last set of data is understood to provide particularly reliable and robust estimates of the star-formation rate because they rather directly trace the emission by young stellar populations and are free of dust extinction effects (Kennicutt 1998; Franceschini et al. 2001; Elbaz et al. 2002). The blue star symbol at $z \simeq 7$ is the determination of the SFR density of Bunker et al. (2009) from HST-WFC3 data with the z' -drop technique, effective over the redshift range $6.7 < z < 8.8$, as indicated by the x -axis bar.

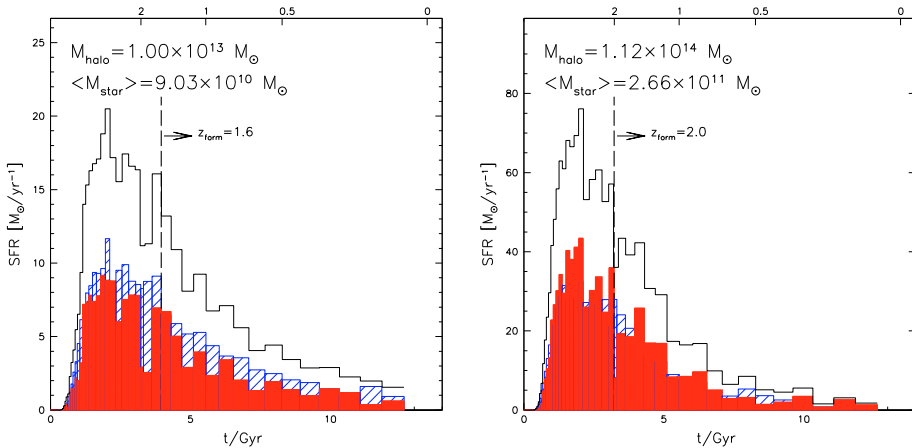
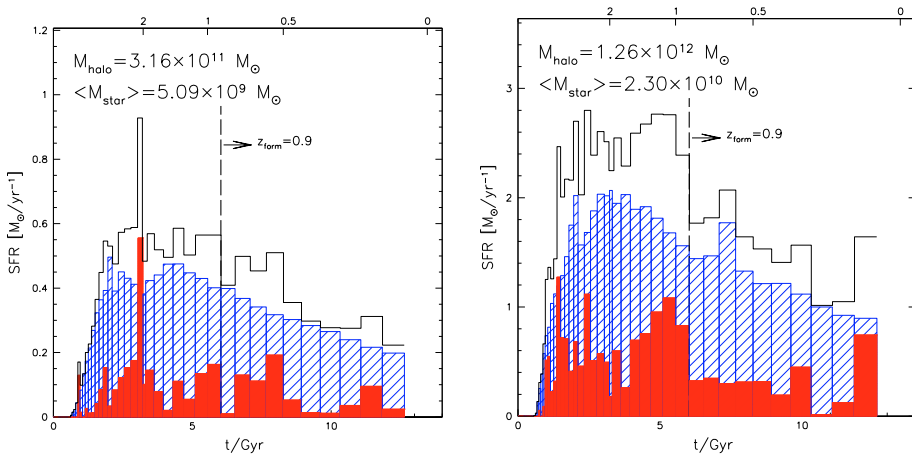
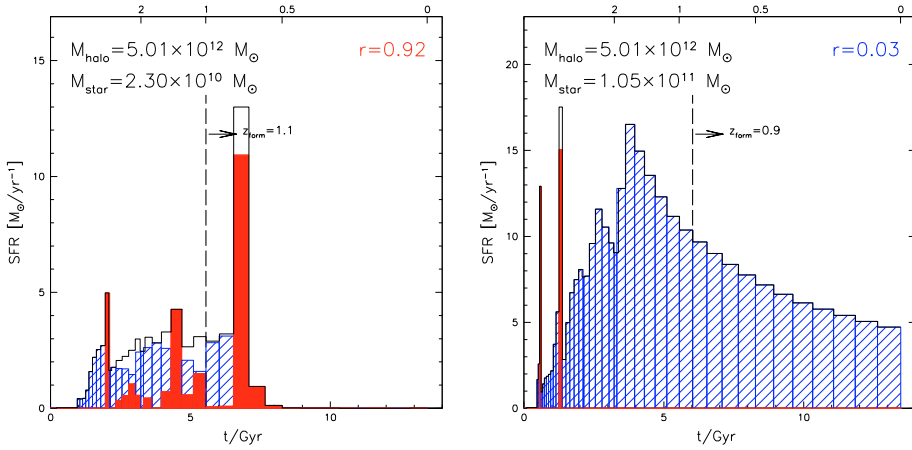
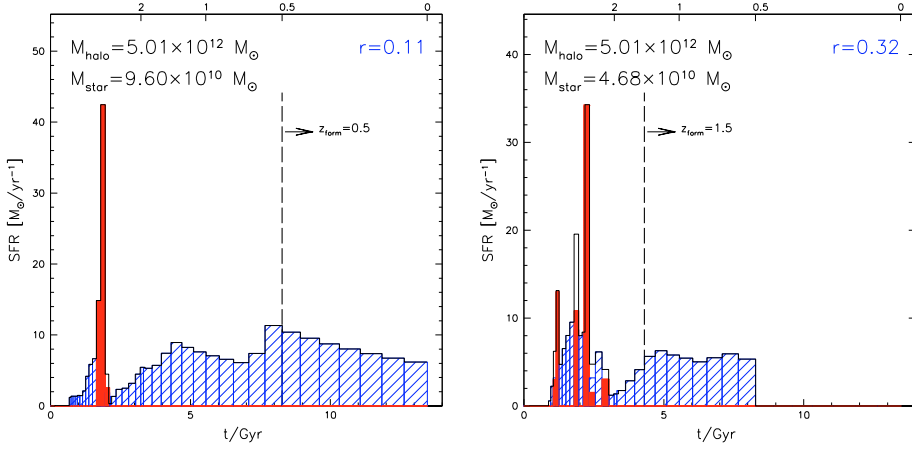


Fig. 7. SFHs of stellar populations for different realizations of the central galaxy of a Milky-Way like halo, having masses equal to $5 \times 10^{12} M_{\odot}$. These SFHs sum up the contributions to the final galaxy stellar mass by all the stars present in the galaxy at $z = 0$. Blue shaded histograms show the star formation occurring in the quiescent mode, the red ones represent the bursty mode, while the black envelope is the total SFR. The vertical dashed line indicates the formation redshift of the galaxy. The final stellar masses in each realizations are indicated.

Fig. 8. Averaged SFHs for central galaxies of 4 different halos, with masses ranging from $\sim 10^{11} M_{\odot}$ to $\sim 10^{14} M_{\odot}$. The average are computed over 100 realizations. As in Fig. 7, blue shaded histograms show the star formation occurring in quiescent mode, the red ones represent the bursty mode, while the black envelope is the total SFR. The host halo mass and the averaged final stellar mass are indicated.

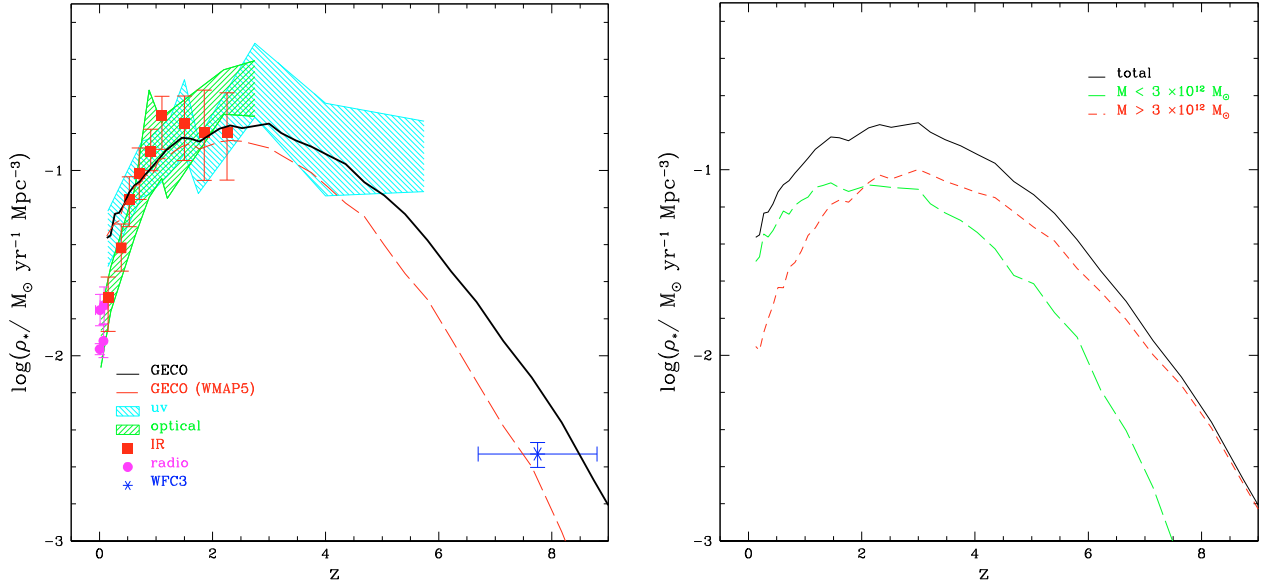


Fig. 9. *Left panel:* SFR density as a function of redshift. Solid black line shows the GECO predictions. The shaded area and coloured points are the SFR obtained from observations at different wavelengths. The cyan shaded region shows the SFR derived from UV tracers, green region means that observations are in the optical, and magenta dots in the radio (from the compilation of Hopkins 2004); red squares refer to infrared determinations, from Rodighiero et al. (2010) and the blue star is the $z \approx 7$ determination from HST-WFC3 data (Bunker et al. 2009). *Right panel:* SFR density divided into the contribution by objects residing in different halo masses. Solid black line shows the total SFR density, red short-dashed shows the contribution from galaxies living in high-mass halos ($M_{\text{halo}} > 3 \times 10^{12} M_\odot$), while the green long-dashed curve represents the contribution from galaxies in less massive halos ($M_{\text{halo}} < 3 \times 10^{12} M_\odot$).

The model provides a remarkably good fit to the data over most of the redshift range. We note, in particular, the close agreement between the model and the IR data, which exhibits a steep rise from $z = 0$ to $z = 1$ and then a wide plateau up to $z \sim 4$. Locally ($z \lesssim 0.2$), there is an indication that our model produces too many stars. Our predictions appear consistent with the UV data, but are higher than the relation of Rodighiero et al. (2010), obtained using the Spitzer $24 \mu\text{m}$ luminosity function. Even at very high redshift ($z \approx 7$), the model is marginally consistent with the observations, especially if we take into account that the HST-WFC3 data can be considered as a lower limit due to incompleteness effects. We also note that the WMAP5 model predicts a much lower SFR at high redshift, ($z \gtrsim 2$) providing closer agreement with the $z \approx 7$ data. In contrast to what was found by Somerville et al. (2008), using the new cosmology we find a closer agreement with data for the SFR density, but a poorer one in the stellar mass assembly, as noted above.

The high level of star formation rate at redshifts $z \approx 3-5$ found in the model was mentioned in the previous section. On the one hand, the quiescent mode of star formation is very effective, due to the high cooling efficiency in the denser environment. The peak in the quiescent mode of star formation (blue shaded histograms in Figs. 8) is indeed always at $z \sim 2$. On the other hand, at high redshift the star formation mainly occurs in starbursts, triggered by the high merging rate, which enhances the SFR at early cosmic times. The exhaustion of cold gas available explains the sharp later decline at lower redshifts.

In the right panel of Fig. 9, the contribution to the total star formation rate density (black solid line) is divided according to the mass of the hosting halo: the short-dashed red line shows the contribution from galaxies living in high-mass halos ($M > 3 \times 10^{12} M_\odot$), while the green long-dashed line shows that of galaxies living in less massive halos. The time dependence of the star formation rate in the two cases has a similar behaviour: a slow

increase at high redshifts, a phase of peak activity, and finally a rapid decline to the present time. However, in addition to this general pattern, we notice a systematic shift in the SFR history between the two halo populations, the high-mass halo activity being shifted at higher redshifts, $z \sim 2-4$, while it is more concentrated around $z = 1-2$ in the less massive population.

We then confirm our previously found results: galaxies residing in high-mass halos form their stars at earlier epochs, and their star formation then rapidly slows-down, while galaxies in less massive systems form stars at significant rate even at recent times ($z \lesssim 1$).

6.5. Star formation and mass assembly

We discussed in the previous sections an important aspect of our model, its prediction that massive systems form their stars at earlier times than less massive objects. This however concerns the birth times of the galaxy's stellar populations, while the times of mass assembly may be very different when stars are formed at high redshift in a number of distinct progenitors and are assembled at more recent times.

In Fig. 10 we compare the star formation history with the “assembly history” for single realizations of various parent halos. In the upper boxes of each panel, we show the SFH of all stellar populations contributing to the final galaxy, in analogy with those reported in Fig. 7. The SFH is expressed here in terms of the fraction of the final stellar mass formed in each time-step (instead of the SFR), for an easier quantitative comparison with the assembly history. In the bottom boxes, we show the mass assembled into the main progenitor at each time-step, where the main progenitor identifies at each redshift the progenitor of the galaxy that survives until the present day. Here, red histograms indicate the amount of stars added to the bulge in a given time-step, while blue histograms show the stars added to the disc.

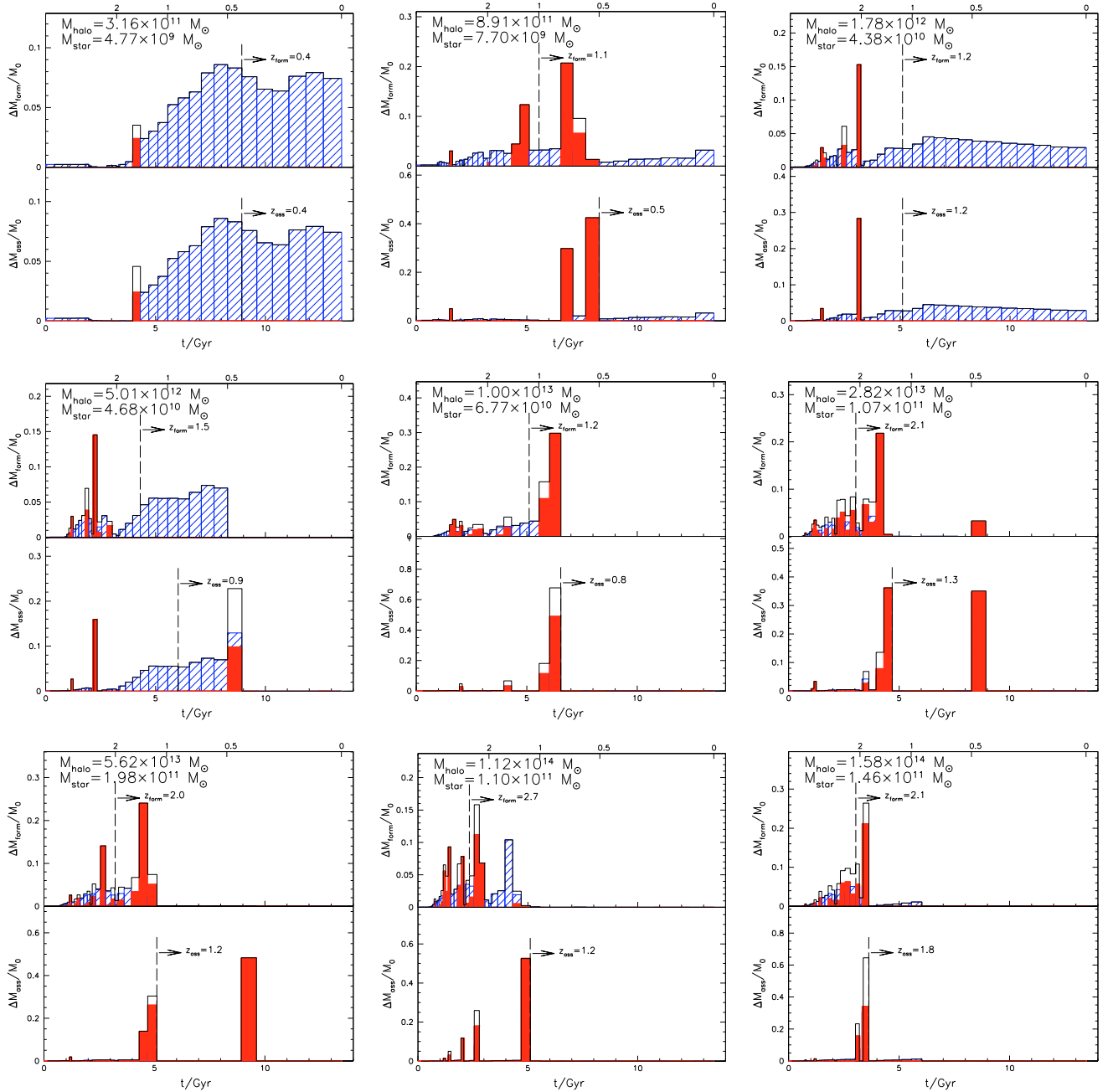


Fig. 10. Comparison between stellar mass formed (*upper panels*) and assembled into the main progenitor (*lower panels*) for different model galaxies, living in different halos. In the *upper panel*, red and blue histograms represent, respectively, bursty and quiescent SF, while in the *assembly panels* red and blue stay for the mass assembly of bulges and discs respectively.

Although in a few cases the history of stellar assembly is very similar to that of star formation, indicating that star formation took place mainly in one single object, in general the two paths can differ significantly.

In most cases, the assembly of bulges, due to mergers, is related to starbursts, although in some systems, mainly in merging episodes at low redshifts, the mass assembly is not associated to any event of star formation because the gas content is already consumed (*dry merging*). Substantial dissipationless merging may lead to very different formation times for the processes of star formation and mass build-up. Although dry mergers in the local universe are observed, their frequency and role in galaxy evolution are still poorly constrained by observations (van Dokkum 2005; Bell et al. 2006). Galaxy formation models

do however predict that they are a crucial process in the formation of local ellipticals (see Cattaneo et al. 2010).

We define the redshift of assembly as that corresponding to when half of the final stellar mass is assembled in one single object, and show this in Fig. 10. By definition, the assembly redshift is always lower than the formation one, and they equal each other when almost all the stars are formed in the main progenitor.

In Fig. 11, we report the dependences of the mean star-formation redshift (*upper panels*) and the redshift of mass assembly (*lower panels*) on both the hosting halo mass (left-hand panels) and of the galactic stellar mass (right-hand panels). Errorbars indicate the standard error in the mean over 100 MC realizations of the same host halo. We note that to derive the redshift of formation (or assembly) as a function of stellar mass we

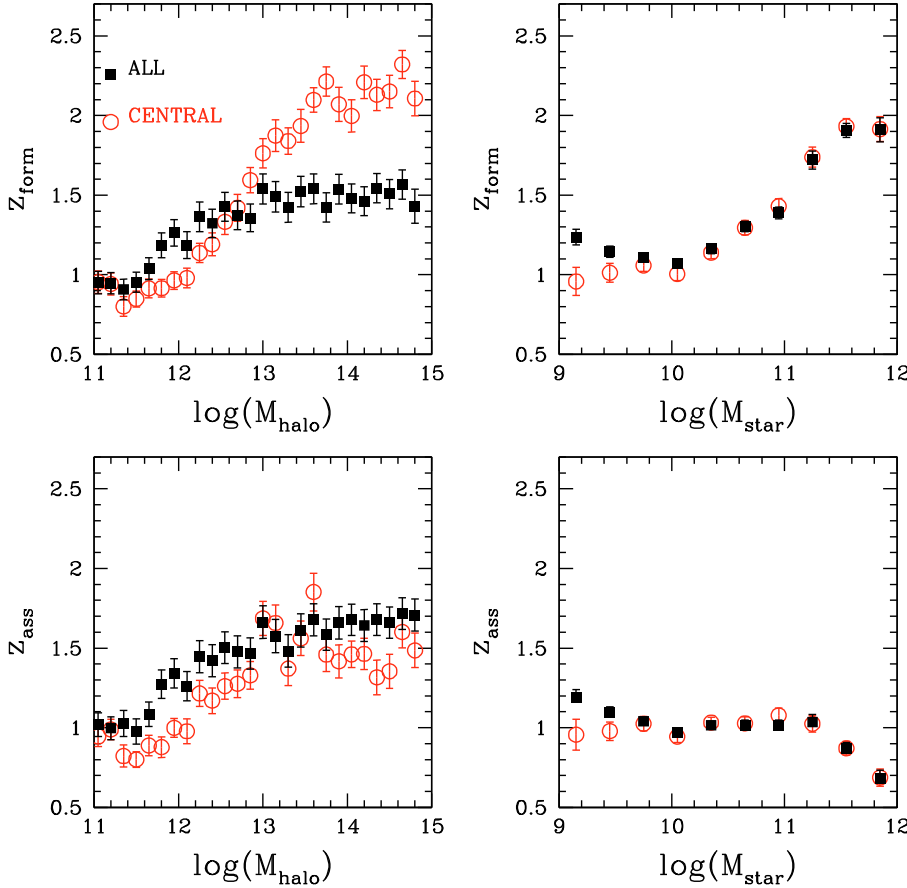


Fig. 11. Mean formation redshift (*upper panels*) and assembly redshift (*lower panels*) of galaxies as a function of their host halo mass (*left-hand panels*) and stellar mass (*right-hand panels*). Black squares indicate the global population of galaxies, including central and satellites, while red open circles represent central galaxies. Error-bars indicate the standard error in the mean over 100 MC realizations of the same halo.

weight each galaxy mass by the number density of its host halo, because any stellar mass may belong to a certain range of halo masses.

The mean formation redshift exhibits a clear increase with both halo and stellar mass. This effect is more pronounced for the central galaxies than for the whole population including satellites. We have already shown in the previous sections how galaxies living in high-mass halos formed their stars earlier and at a higher rate than in low-mass halos. Here, we demonstrate that the trend is also true for the galactic stellar mass, although it is weaker. We note that the most massive halos ($M_{\text{halo}} > 10^{14} M_{\odot}$) host galaxies with a higher formation redshift ($z_{\text{form}} \sim 2.5$, top left panel of the figure), but since these halos are very rare, the mean formation redshift of the more massive galaxies ($M_{\text{star}} \sim 10^{12} M_{\odot}$), which belong to a certain range of halo masses, remains somewhat lower (~ 2 , top right panel).

The behaviour of the redshift of mass assembly is more difficult to interpret. We found that, on average, galaxies living in high mass halos assemble their stars earlier. The merger timescales related to both dynamical friction and random collisions among satellites indeed increase with the halo mass. We already mentioned in Sect. 3.6.1 that the dynamical friction time increases with the ratio of the mass of the halo to that of the satellite (Eq. (23)). Moreover, since the merger probability is significantly lower for high-velocity encounters, the merger rate for satellites decreases with the ratio V_c/v_{gal} (Eq. (24)), and becomes very low for massive cluster-size halos. Nevertheless, when the redshift of mass assembly is expressed in terms of the galactic stellar mass, the downsizing behaviour is no more recovered: the assembly time keeps approximately constant around $z_{\text{ass}} \sim 1$ for low and intermediate masses and decreases in the highest mass end, with $z_{\text{ass}} \sim 0.7$ for $M_{\text{star}} \sim 10^{12} M_{\odot}$. These stellar mass

values correspond to those of the cD galaxies in local rich clusters or groups. The combined effects of the formation redshift and the assembly redshift suggest that the only way of forming the most massive galaxies in the local universe is in the form of dry mergers at recent times. Massive galaxies indeed cease to form stars quite early and, without these events, they are unable to grow their mass above $M_{\text{star}} \simeq 10^{11} M_{\odot}$.

In conclusion, our model expectation is that, although mergers and collisions are rare in massive halos, they do occur, and their effect is crucial in the formation of today's most massive galaxies. Refined observational estimates of the galaxy mass functions at the high mass-end throughout the $z = 0$ to 4 redshift interval (on top of those already apparent in Fig. 5) will clarify how far this expectation of a substantial *dry merging* process is borne out by the data.

7. Discussion and conclusions

We have presented a new semi-analytical model of galaxy formation, the Galaxy Evolution Code, GECCO, which appears to reproduce several key statistical properties of local and high-redshift galaxies.

GECCO uses a state-of-the-art Monte Carlo algorithm to represent the dark matter halo merging history that is based on the extended Press-Schechter formalism. GECCO includes detailed implementations of gas cooling, star formation, feedback from SN, and galaxy mergers, caused by both dynamical friction and random collisions. The parallel growth of BHs is followed in time and the subsequent AGN feedback is modelled.

We tested our results directly for observables related to the stellar mass and star-formation rate, rather than luminosity, as usually done by other published models. This is because on

the one hand the stellar mass functions are the most direct outcome of the model. On the other hand, stellar masses in galaxies have become a straightforward observable thanks to rest-frame near-infrared data from the Spitzer Space Telescope, which directly probes the stellar mass content in high-redshift galaxies. At the same time, Spitzer also helps us to measure with deep far-infrared photometric imaging the rate of star-formation rate of distant objects. We can therefore compare the outcomes of our model with the most reliable set of observables and a minimal number of free parameters. We thus believe that the basic physics of the Λ CDM hierarchical clustering concept of galaxy formation can be tested by ourselves in a very effective way.

The main results obtained in the present work are summarised in the following:

1. The local stellar mass function is in a remarkably good agreement with the determination of [Cole et al. \(2001\)](#) and [Bell et al. \(2003\)](#) (Fig. 2). At the high-mass end, the total mass function is dominated by the contribution of bulges, while discs dominate at the faint-end. When the total stellar mass is divided into the contributions of early-type and late-type galaxies, the former populate the bright-end side, while the latter mainly contribute at low masses. The number densities of the two morphological types cross each other at $M_{\text{star}} \sim 3 \times 10^{10} M_{\odot} h^{-1}$, as observed. Although we reproduce the general trend of the morphological mass functions, our model fails to match the low-mass end of spheroids, showing an excess of low-mass systems. This is most likely caused by an oversimplification of the satellite population, since satellite galaxies lose their hot gas reservoir as soon as they are incorporated into a more massive halo and the star formation is quenched soon after.
2. The co-evolution of galaxies and BHs has been modelled following the prescriptions of [Croton et al. \(2006\)](#). A first mode of accretion onto BHs considered is the so-called “radio-mode”, which inhibits the quiescent star formation, while the second one is the “QSO-mode”, which is triggered only during galaxy mergers and constitutes a major channel of BH accretion. As a consequence of mergers, a starburst is also induced, feeding the galactic bulge component (and destroying the disc in the case of a major merger). This leads to both a parallel growth of BH and bulges with the two masses being very well correlated, in agreement with observational data ([Håring & Rix 2004](#)), and a the local black-hole mass function in remarkable agreement with the observations of ([Shankar et al. 2004](#)).
3. We compared the stellar mass functions predicted by the model with various observational determinations up to $z \sim 3.5$ (Fig. 5) and found a reasonably close agreement over the whole redshift range considered. Nevertheless, the observed ratio of the evolution of the faint- to the bright-end of the stellar mass function is not very accurately reproduced: there is too much evolution in the model at the bright-end and too little at the faint-end compared to observations. Various sets of observables indicate a large increase in the number density of low-mass objects between $z \sim 2$ and the present day and a lower rate of evolution for massive objects. However, we mentioned that the completeness and robustness of the observational mass function are to be proven there, before claiming more definite conclusions. In the case of a WMAP5 cosmology, we observe a delay in the formation of cosmic structure, which leads to an additional reduction of high-mass systems.
4. The bolometric quasar luminosity function is compared with [Hopkins et al. \(2007a\)](#), showing a good level of agreement at low and intermediate redshift, but a tendency to underpredict the number of bright quasars at high redshift. A mechanism for enhancing the cooling rate at high redshift might simultaneously increase the fuel for BHs and enhance the SF at high redshift, as seems to be required to improve the match with the stellar mass functions.
5. The integrated star formation rate density (Fig. 9) shows a high level of star formation at high redshifts, a peak at $z \sim 1.5-3$, and then a sharp decline below $z \sim 1$. When compared with the determination of the SFH derived using various tracers (UV, optical, radio, IR), our predictions are in very close agreement with these observations. At very high redshift ($z \approx 7$), our model is able to correctly reproduce the most recent determination of the SFR density by HST-WFC3 data.
6. We analysed in detail the SFH in simulated sets of galaxies, to obtain insight into how the model treats star formation and how it depends on the galaxy or halo mass. We computed the average SFH for the central galaxies living in halos of different sizes (Fig. 8). We identified two main trends with halo mass. First, when going to high-mass systems, the contribution of the starburst mode to the total SF becomes increasingly important, and indeed predominant in very high mass objects. Second, the formation redshift, defined as that when half of the present-day stellar mass is formed, increases, leading to older stellar populations in massive systems. Hence galaxies in our model form their stars following a *downsizing* pattern, consistent, for instance, with the dating of stellar populations in local galaxies ([Thomas et al. 2005](#)). The naive expectation of early versions of hierarchical galaxy formation models was that, since massive halos are assembled later than their lower-mass counterparts, the most massive galaxies, hosted in the largest halos, should form their stellar content at the same late cosmic time. As shown in Fig. 11, this is clearly, however, not the case in our refined model, according to which, *downsizing* in star formation is an intrinsic feature of semi-analytical models (see also [Neistein et al. 2006](#)). The present-day massive galaxies were formed by the assembly of a number of smaller progenitors that collapsed at high redshifts from the highest density peaks of the primordial density field. According to this scenario, also called biased galaxy formation ([Dekel & Silk 1986](#)), bright and massive systems started to form begins early on. This is a natural outcome of the merger tree formalism: progenitors of high-mass halos fall below the resolution mass imposed on the merger tree after several time-steps back in cosmic time, so the “leaves of the tree” are found at high redshift. In contrast, smaller systems, closer to the resolution mass, take only a few time-steps back to reach this minimum mass. We note that this is not merely a computational artifact, but is because there should be quite negligible star formation below such threshold mass, due to the SF quenching by the UV photoionizing background (Sect. 3.5.2). Since baryons are put into halos starting from the leaves, in high-mass halos, star formation took place at early times. Moreover, at high redshift both mechanisms of star formation were more effective than at low redshift. Thanks to the efficient cooling of the gas, the quiescent mode of star formation occurs at an enhanced rate. The frequency of mergers at these times is also high, allowing an efficient conversion of gas in stars via a starburst. The exhaustion of cold gas is, therefore, very rapid, leaving

the galaxy devoid of fuel, and preventing additional star formation occurring.

Another reason for star-formation quenching in massive systems may be ascribed to AGN feedback. To check the importance of this mechanism, we performed a test simulation with the AGN emission switched off. The comparison between the two versions of the model are presented in Appendix A. We found that AGN feedback has some effect in increasing the average age of stellar populations in the most massive galaxies, as pointed out by previous works (Croton et al. 2006; De Lucia et al. 2006; Cattaneo et al. 2008). However, in our model the *downsizing* trend is recovered, although slightly weaker, even in the absence of an AGN.

Therefore, in GECO, the AGN feedback does not have a dramatic effect in producing the local galaxy properties (see also Menci et al. 2006; and Monaco et al. 2007), and it is not the main reason for the *downsizing* pattern of galaxy evolution. In our modelling, the latter trend is due instead to a higher efficiency of SF back in time for the most massive galaxies in the richest environments, as explained above. Although we have shown that the *downsizing* is quite a natural feature of our model, it is not the case for all the published models and some of them fail to reproduce this trend with mass, as shown in Fontanot et al. (2009).

7. Finally, we compared the star-formation history of simulated galaxies with the mass-assembly history, that is the history of the mass assembled into the main progenitor at each time-steps (Fig. 10). As expected, the two processes can occur on very different timescales, especially in high-mass systems, for which the star formation took place at high redshift in many distinct progenitors, that combined at low redshift. The late assembly of these systems occurs in the majority of the cases through *dry mergers*, i.e., mergers between spheroidal systems with little or no gas. In these cases, the merger is accompanied by no star-formation event, neither quiescent nor bursting. An intriguing question is then whether galaxies in the model assemble their stellar mass in a *downsizing* way, as occurs for the star formation. Possible downsizing effects in the mass assembly were indicated by several authors (Bundy et al. 2006; Cimatti et al. 2006; Hopkins et al. 2007b) as inferred from the lack of evolution in the high-mass end of the mass function and by the evolution of the blue-to-red galaxy crossover mass (the mass for which the early-type mass function intersects that of late-types). In our model, we found that although the assembly time shows a shallow dependence on the host halo mass, galaxies living in massive halos on average assemble their stars before galaxies in less massive hosts (Fig. 11). The assembly times are almost constant with stellar mass, and are lower for very-high mass systems ($M_{\text{star}} > 10^{11} M_{\odot}$), leading to an *upsizing* trend with time in the high-mass end. In our modelling, dry mergers are the main reason for this late assembly of massive galaxies. These findings agree with other previously published semi-analytical models (De Lucia et al. 2006; Cattaneo et al. 2008, 2010). The importance of dry mergers in forming the most massive galaxies that we observe in the nearby universe, is also implied by the observations of the size evolution of massive spheroids (Trujillo et al. 2007; Cimatti et al. 2008). If these compact galaxies were indeed absent in the local universe as suggested by Trujillo et al. (2009), the mechanisms that move the high-redshift compact galaxies onto the local relation should be dissipationless mergers. However, other studies (Valentinuzzi et al. 2010) find that superdense galaxies are not as rare in the local universe as previously claimed.

How far this might be incongruous with the observational indication of downsizing in mass assembly mentioned above will become clear with further observational confrontation. For example, Cattaneo et al. (2008) argue that the upsizing in mass assembly can coexist with a downward trend in the transition mass, which then turns out to be a poor indicator of downsizing.

In conclusion, GECO presents an encouraging level of agreement with a wide range of observational data, at low and high redshifts. We have focused on comparing GECO with data for the two main phases of the galaxy formation process, which are star formation and mass assembly. On the one hand, we confirmed that the observed *downsizing* in star formation is a natural part of our scheme of hierarchical growth of structures. On the other hand, the stellar mass-assembly process remains more difficult to understand from both a theoretical and an observational point of view. The timescales of galaxy assembly in our model, related with both the galaxy merger timescales and the star-formation efficiency, depend strongly on the details of the implementations of galaxy dynamics (dynamical friction, satellite collisions, and tidal stripping). In this respect additional work is required to obtain a deeper insight into the galaxy assembly process, and certainly a comparison with N -body simulations would be helpful.

The most striking conclusion is that, despite the simplicity of the prescriptions adopted, and the small number of free parameters used, the main features of the evolving galaxy population are reproduced. In particular, the AGN feedback is needed only to improve the match of the local stellar mass function, but its effect on stellar ages is not significant.

We caution that this paper includes just a preliminary and partial confrontation with the data, showing at least no obvious disagreement. Far more extensive analyses and tighter constraints will be obtained as soon as higher quality data on the evolutionary mass functions and stellar birthrates become available.

Acknowledgements. We thank the referee for helpful suggestion which improved the paper. We are grateful to Nicola Menci for various illuminating discussions, criticisms and suggestions about the present model. We also thank Alfonso Cavaliere and Pierluigi Monaco for discussions and Antonio Cava, Carlo Giocoli and Ignacio Trujillo for helpful suggestions. We acknowledge financial support by the Padova University for the PhD studentship and the Italian Space Agency for funding a post-doc fellowship, which made this paper possible.

Appendix A: Effect of AGN feedback

Several recent works (Croton et al. 2006; Malbon et al. 2007; Sijacki et al. 2007) advocated the AGN feedback as the only mechanism capable of quenching star formation to match the local abundance of massive galaxies as well as their old ages and red colours. Here we check the relevance of this feedback in reproducing the observations in GECO, by comparing our fiducial model with a version in which the AGN feedback (both in quasar and radio modes) is switched off. In Fig. A.1, we can see the effect of AGN feedback in the stellar mass function. As expected, the presence of the AGN influences only the bright-end, reducing it by ≈ 0.15 dex, both in the local universe (upper panel) and at high redshift (lower panel), hence leading to the same amount of evolution in the stellar mass function as in the fiducial case. We note that given the overabundance of massive galaxies by the same amount at all redshifts, in the model without AGN, the comparison with the observational mass function at high redshift results in a closer agreement with the fiducial model. Figure A.2

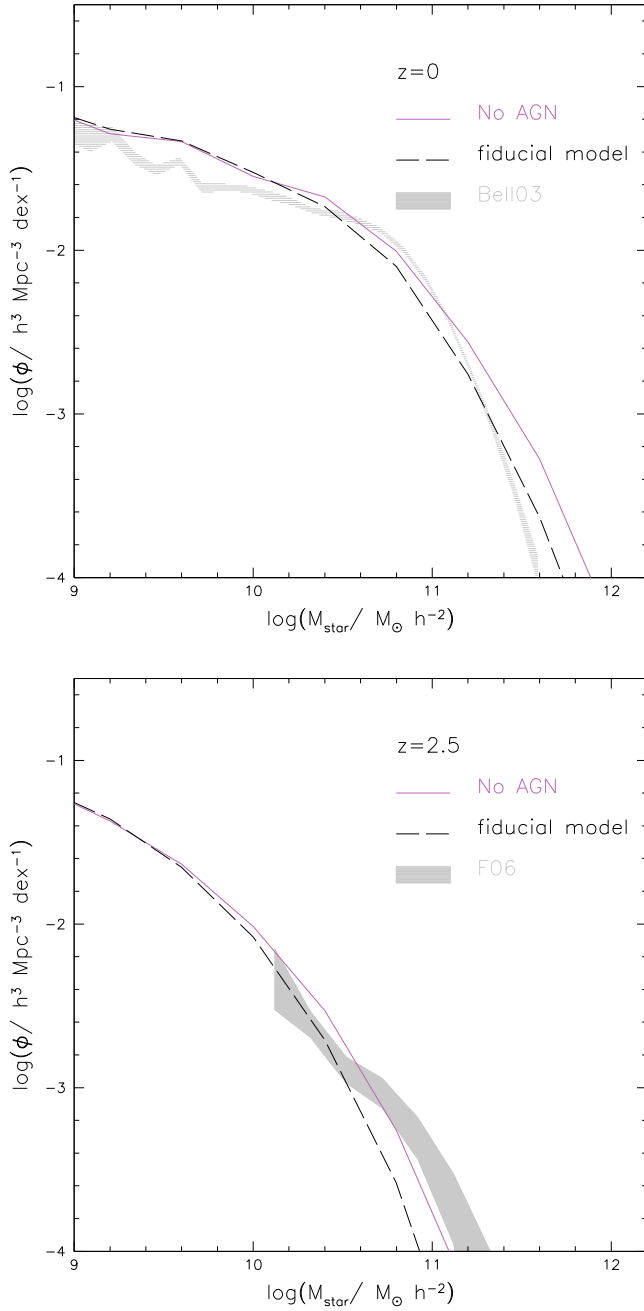


Fig. A.1. *Upper panel:* comparison between the stellar mass function at $z = 0$ of our fiducial model (dashed black line) with the model without AGN feedback (solid purple line). *Lower panel:* the same as the *upper panel* but for $z = 2.5$. Observational data at the given redshift are also indicated by the shaded region.

shows that, obviously, in the model without AGN the star formation keeps a lower level at all redshifts, with an indication that at very high redshift ($z > 4$) the difference between the two models tends to disappear, meaning that the importance of AGN feedback increases at late cosmic times.

An additional issue to be handled is the relevance of the AGN in producing the downsizing trend in the stellar ages. In Fig. A.3, the trend of the formation redshift with mass is shown for both models. Although the AGN feedback is effective in increasing stellar ages, the net effect is actually very modest. At variance with other models (Croton et al. 2006, for instance), the downsizing trend is still recovered, leading to the conclusion that the

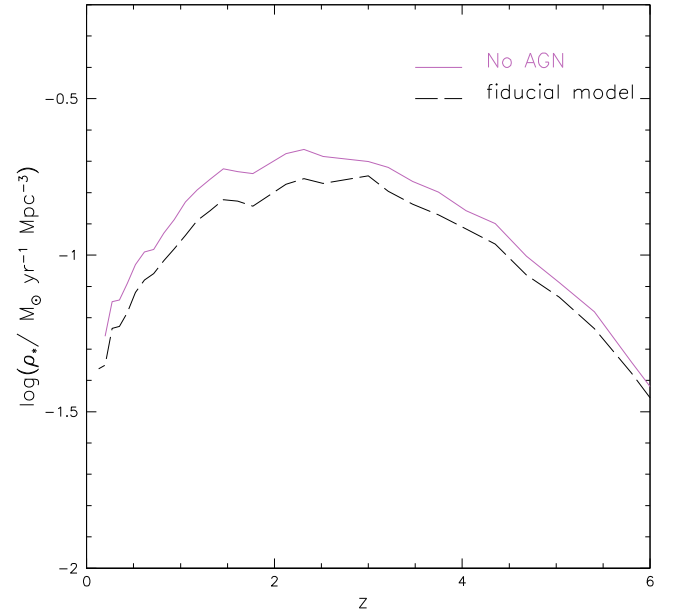


Fig. A.2. Comparison between the SFR density as a function of redshift in the model without AGN feedback (solid purple line) and the fiducial case (dashed black line).

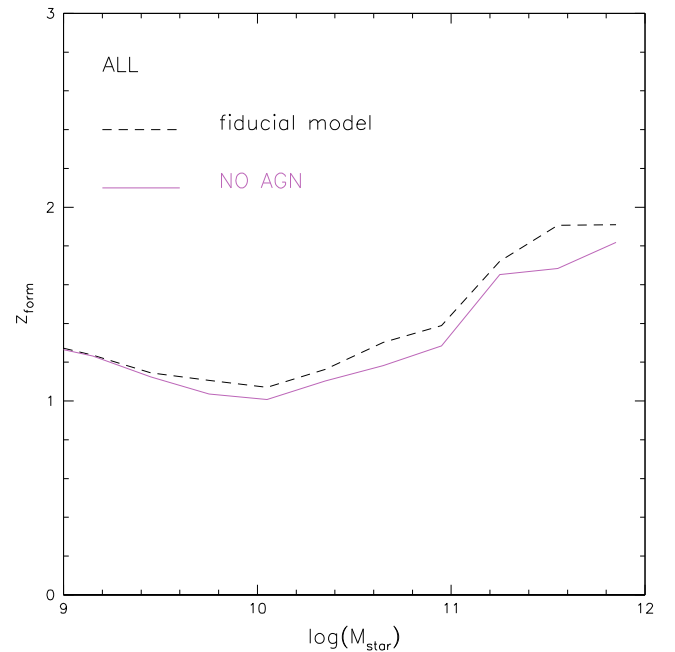


Fig. A.3. Comparison between the formation redshifts as a function of stellar mass in the model without AGN feedback (solid purple line) and the fiducial case (dashed black line).

presence of AGN is not the main reason for the onset of the downsizing pattern for galaxy evolution in our model.

Therefore, in our model the AGN has the effect of reducing the star formation activity in the high-mass objects, but the amount of reduction is perhaps less striking than previously claimed (Croton et al. 2006; Malbon et al. 2007; Marulli et al. 2008; Lagos et al. 2008). The efficiencies of black-hole accretion adopted here, are somewhat lower than those adopted by the models mentioned above, but we found that they are suitable for obtaining a very good match with the local relations.

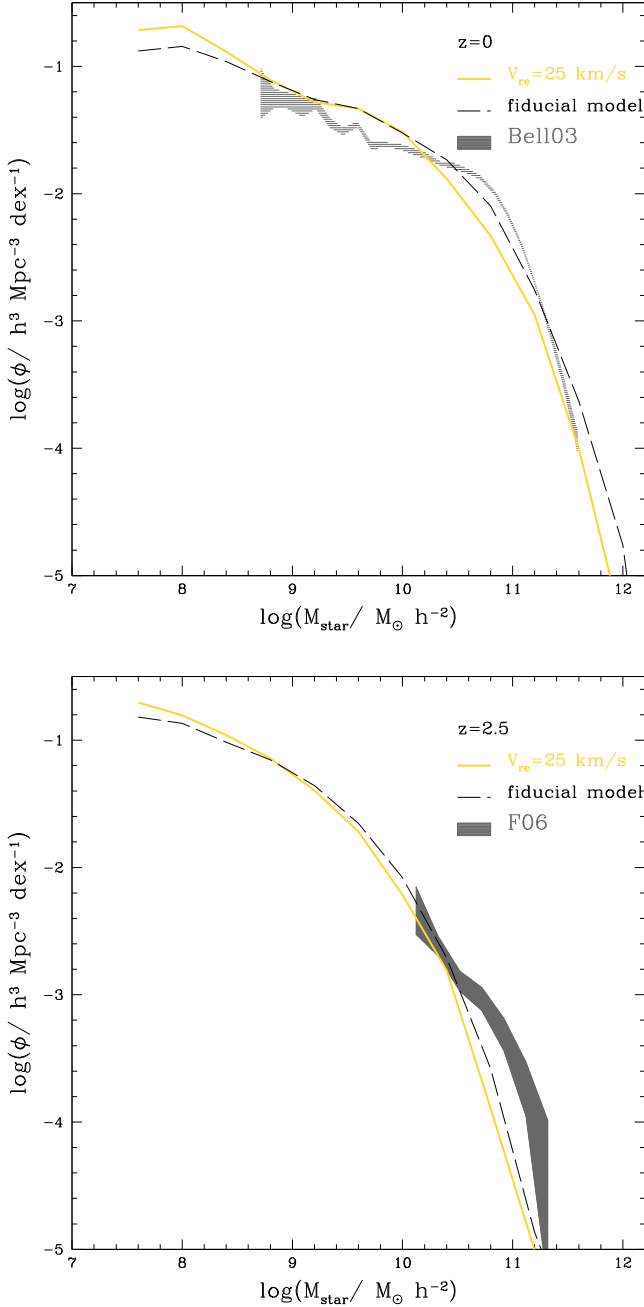


Fig. B.1. *Upper panel:* comparison between the stellar mass function at $z = 0$ of our fiducial model (dashed black line) with a model with a reduced effect of the cosmic reionization (solid yellow line). *Lower panel:* the same as the upper panel but for $z = 2.5$. Observational data at the given are also indicated by the shaded region.

Appendix B: Effect of cosmic reionization

As explained in Sect. 3.5.2, our treatment of the cosmic reionization is based on the results of Benson et al. (2003). However, it has been claimed, on the basis of hydrodynamical simulations, that the effect of the photoionizing background on structure formation is indeed weaker than previously assumed (Hoeft et al. 2006; Okamoto et al. 2008). Taking into account these results, we test the effect of our assumptions on the limiting circular velocity for the reionization. In Fig. B.1 we compare our fiducial model with a model in which the circular velocity limit for baryon cooling has been lowered to 25 km s^{-1} . To allow the formation of low-mass halos, we used in this model a merger tree

with a resolution of $10^9 M_{\odot}$. We see that a lower limit on the circular velocity has the effect of slightly increasing the number of low-mass galaxies. At the same time, the number of massive objects is reduced, since a greater amount of gas has been locked within satellites and is not available for star formation inside the brightest systems. In any case, the effect is rather moderate and the prediction of the fiducial model could be accommodated, for instance, by increasing the effect of SN.

Therefore, we conclude that although we might have overestimated the effect of reionization in our fiducial model, the main results found in the previous sections remain unchanged if we allow a milder dependence of galaxy formation on the cosmic reionization.

References

- Baldry, I. K., Glazebrook, K., Brinkmann, J., et al. 2004, *ApJ*, 600, 681
 Baugh, C. M., Cole, S., & Frenk, C. S. 1996, *MNRAS*, 283, 1361
 Bell, E. F., McIntosh, D. H., Katz, N., & Weinberg, M. D. 2003, *ApJS*, 149, 289
 Bell, E. F., Phelps, S., Somerville, R. S., et al. 2006, *ApJ*, 652, 270
 Benson, A. J., Lacey, C. G., Baugh, C. M., Cole, S., & Frenk, C. S. 2002, *MNRAS*, 333, 156
 Benson, A. J., Frenk, C. S., Baugh, C. M., Cole, S., & Lacey, C. G. 2003, *MNRAS*, 343, 679
 Berta, S., Lonsdale, C. J., Polletta, M., et al. 2007, *A&A*, 476, 151
 Bertone, S., De Lucia, G., & Thomas, P. A. 2007, *MNRAS*, 379, 1143
 Blumenthal, G. R., Faber, S. M., Primack, J. R., & Rees, M. J. 1984, *Nature*, 311, 517
 Bond, J. R., & Myers, S. T. 1996, *ApJS*, 103, 1
 Bond, J. R., Cole, S., Efstathiou, G., & Kaiser, N. 1991, *ApJ*, 379, 440
 Bower, R. G., Benson, A. J., Malbon, R., et al. 2006, *MNRAS*, 370, 645
 Boylan-Kolchin, M., Ma, C.-P., & Quataert, E. 2008, *MNRAS*, 383, 93
 Bundy, K., Ellis, R. S., & Conselice, C. J. 2005, *ApJ*, 625, 621
 Bundy, K., Ellis, R. S., Conselice, C. J., et al. 2006, *ApJ*, 651, 120
 Bunker, A., Wilkins, S., Ellis, R., et al. 2009, *MNRAS*, in press [arXiv:0909.2255]
 Cattaneo, A., Dekel, A., Devriendt, J., Guiderdoni, B., & Blaizot, J. 2006, *MNRAS*, 370, 1651
 Cattaneo, A., Dekel, A., Faber, S. M., & Guiderdoni, B. 2008, *MNRAS*, 858
 Cattaneo, A., Mamon, G. A., Warnick, K., & Knebe, A. 2010, *MNRAS*, submitted [arXiv:1002.3257]
 Chandrasekhar, S. 1943, *ApJ*, 97, 255
 Cimatti, A., Daddi, E., & Renzini, A. 2006, *A&A*, 453, L29
 Cimatti, A., Cassata, P., Pozzetti, L., et al. 2008, *A&A*, 482, 21
 Croton, D. J., Springel, V., White, S. D. M., et al. 2006, *MNRAS*, 365, 11
 Cole, S., & Lacey, C. 1996, *MNRAS*, 281, 716
 Cole, S., Aragon-Salamanca, A., Frenk, C. S., Navarro, J. F., & Zepf, S. E. 1994, *MNRAS*, 271, 781
 Cole, S., Benson, A., Baugh, C., Lacey, C., & Frenk, C. 2000, *ASPC*, 200, 109
 Cole, S., Norberg, P., Baugh, C. M., et al. 2001, *MNRAS*, 326, 255
 Cowie, L. L., Songaila, A., Hu, E. M., & Cohen, J. G. 1996, *AJ*, 112, 839
 Cox, T. J., Jonsson, P., Somerville, R. S., Primack, J. R., & Dekel, A. 2008, *MNRAS*, 384, 386
 De Lucia, G., Kauffmann, G., Springel, V., et al. 2004, *MNRAS*, 348, 333
 De Lucia, G., Springel, V., White, S. D. M., Croton, D., & Kauffmann, G. 2006, *MNRAS*, 366, 499
 Dekel, A., & Birnboim, Y. 2006, *MNRAS*, 368, 2
 Dekel, A., & Silk, J. 1986, *ApJ*, 303, 39
 Dunkley, J., Komatsu, E., Nolta, M. R., et al. 2009, *ApJS*, 180, 306
 Elbaz, D., Cesarsky, C. J., Chial, P., et al. 2002, *A&A*, 384, 848
 Fan, X., White, R. L., Davis, M., et al. 2000, *AJ*, 120, 1167
 Ferrarese, L., & Merritt, D. 2000, *ApJ*, 539, L9
 Fontana, A., Salimbeni, S., Grazian, A., et al. 2006, *A&A*, 459, 745
 Fontanot, F., De Lucia, G., Monaco, P., Somerville, R. S., & Santini, P. 2009, *MNRAS*, 397, 1776
 Franceschini, A., Silva, L., Fasano, G., et al. 1998, *ApJ*, 506, 600
 Franceschini, A., Aussel, H., Cesarsky, C. J., Elbaz, D., & Fadda, D. 2001, *A&A*, 378, 1
 Franceschini, A., Rodighiero, G., Cassata, P., et al. 2006, *A&A*, 453, 397
 Gavazzi, G., & Scodreggio, M. 1996, *A&A*, 312, L29
 Gebhardt, K., Bender, R., Bower, G., et al. 2000, *ApJ*, 539, L13
 Giocoli, C., Moreno, J., Sheth, R. K., & Tormen, G. 2007, *MNRAS*, 376, 977
 Gnedin, N. Y. 2000, *ApJ*, 542, 535
 Häring, N., & Rix, H.-W. 2004, *ApJ*, 604, L89

- Hatton, S., Devriendt, J. E. G., Ninin, S., et al. 2003, *MNRAS*, 343, 75
- Heckman, T. M. 2001, *ASPC*, 240, 345
- Hoefl, M., Yepes, G., Gottlöber, S., & Springel, V. 2006, *MNRAS*, 371, 401
- Hopkins, A. M. 2004, *ApJ*, 615, 209
- Hopkins, P. F., Richards, G. T., & Hernquist, L. 2007a, *ApJ*, 654, 731
- Hopkins, P. F., Bundy, K., Hernquist, L., & Ellis, R. S. 2007b, *ApJ*, 659, 976
- Jiang, C. Y., Jing, Y. P., Faltenbacher, A., Lin, W. P., & Li, C. 2008, *ApJ*, 675, 1095
- Kang, X., & van den Bosch, F. C. 2008, *ApJ*, 676, L101
- Kauffmann, G., & White, S. D. M. 1993, *MNRAS*, 261, 921
- Kauffmann, G., & Haehnelt, M. 2000, *MNRAS*, 311, 576
- Kauffmann, G., White, S. D. M., & Guiderdoni, B. 1993, *MNRAS*, 264, 201
- Kauffmann, G., Colberg, J. M., Diaferio, A., & White, S. D. M. 1999, *MNRAS*, 307, 529
- Kauffmann, G., Heckman, T. M., White, S. D. M., et al. 2003, *MNRAS*, 341, 54
- Kennicutt, R. C., Jr. 1998, *ApJ*, 498, 541
- Kereš, D., Katz, N., Weinberg, D. H., & Davé, R. 2005, *MNRAS*, 363, 2
- Kimm, T., Somerville, R. S., Yi, S. K., et al. 2009, *MNRAS*, 394, 1131
- Kitzbichler, M. G., & White, S. D. M. 2006, *MNRAS*, 366, 858
- Kravtsov, A. V., Gnedin, O. Y., & Klypin, A. A. 2004, *ApJ*, 609, 482
- Lacey, C., & Cole, S. 1993, *MNRAS*, 262, 627
- Lagos, C. D. P., Cora, S. A., & Padilla, N. D. 2008, *MNRAS*, 388, 587
- Lanzoni, B., Guiderdoni, B., Mamon, G. A., Devriendt, J., & Hatton, S. 2005, *MNRAS*, 361, 369
- Lapi, A., Shankar, F., Mao, J., et al. 2006, *ApJ*, 650, 42
- Macciò, A. V., Kang, X., Fontanot, F., et al. 2010, *MNRAS*, 402, 1995
- Malbon, R. K., Baugh, C. M., Frenk, C. S., & Lacey, C. G. 2007, *MNRAS*, 382, 1394
- Mamon, G. A. 1992, *ApJ*, 401, L3
- Marchesini, D., van Dokkum, P. G., Förster Schreiber, N. M., et al. 2009, *ApJ*, 701, 1765
- Martin, C. L. 1999, *ApJ*, 513, 156
- Marulli, F., Bonoli, S., Branchini, E., Moscardini, L., & Springel, V. 2008, *MNRAS*, 385, 1846
- McCarthy, I. G., Frenk, C. S., Font, A. S., et al. 2008, *MNRAS*, 383, 593
- Menci, N., & Cavaliere, A. 2002, *ASPC*, 253, 429
- Menci, N., Cavaliere, A., Fontana, A., et al. 2004, *ApJ*, 604, 12
- Menci, N., Fontana, A., Giallongo, E., Grazian, A., & Salimbeni, S. 2006, *ApJ*, 647, 753
- Mihos, J. C., & Hernquist, L. 1994, *ApJ*, 425, L13
- Mihos, J. C., & Hernquist, L. 1996, *ApJ*, 464, 641
- Mo, H. J., Mao, S., & White, S. D. M. 1998, *MNRAS*, 295, 319
- Monaco, P., Fontanot, F., & Taffoni, G. 2007, *MNRAS*, 375, 11189
- Monaco, P., Fontanot, F., Lo Faro, B., et al. 2009, *AIPC*, 1111, 48
- Navarro, J. F., & White, S. D. M. 1994, *MNRAS*, 267, 401
- Navarro, J. F., Frenk, C. S., & White, S. D. M. 1995, *MNRAS*, 275, 56
- Navarro, J. F., Frenk, C. S., & White, S. D. M. 1997, *ApJ*, 490, 493
- Neistein, E., van den Bosch, F. C., & Dekel, A. 2006, *MNRAS*, 372, 933
- Okamoto, T., Gao, L., & Theuns, T. 2008, *MNRAS*, 390, 920
- Percival, W. J., Sutherland, W., Peacock, J. A., et al. 2002, *MNRAS*, 337, 1068
- Pérez-González, P. G., Rieke, G. H., Villar, V., et al. 2008, *ApJ*, 675, 234
- Perlmutter, S., Turner, M. S., & White, M. 1999, *PhRvL*, 83, 670
- Press, W. H., & Schechter, P. 1974, *ApJ*, 187, 425
- Riess, A. G., Filippenko, A. V., Challis, P., et al. 1998, *AJ*, 116, 1009
- Rodighiero, G., Vaccari, M., Franceschini, A., et al. 2010, *A&A*, 515, A8
- Roos, N., & Norman, C. A. 1979, *A&A*, 76, 75
- Sanders, D. B., & Mirabel, I. F. 1996, *ARA&A*, 34, 749
- Shankar, F., Salucci, P., Granato, G. L., De Zotti, G., & Danese, L. 2004, *MNRAS*, 354, 1020
- Sheth, R. K., & Lemson, G. 1999, *MNRAS*, 305, 946
- Sheth, R. K., & Tormen, G. 2002, *MNRAS*, 329, 61
- Sijacki, D., Springel, V., di Matteo, T., & Hernquist, L. 2007, *MNRAS*, 380, 877
- Somerville, R. S. 2002, *ApJ*, 572, L23
- Somerville, R. S., & Kolatt, T. S. 1999, *MNRAS*, 305, 1
- Somerville, R. S., & Primack, J. R. 1999, *MNRAS*, 310, 1087
- Somerville, R. S., Primack, J. R., & Faber, S. M. 2001, *MNRAS*, 320, 504
- Somerville, R. S., Hopkins, P. F., Cox, T. J., Robertson, B. E., & Hernquist, L. 2008, *MNRAS*, 391, 481
- Spergel, D. N., Verde, L., Peiris, H. V., et al. 2003, *ApJS*, 148, 175
- Spergel, D. N., Bean, R., Doré, O., et al. 2007, *ApJS*, 170, 377
- Springel, V., Yoshida, N., & White, S. D. M. 2001, *NewA*, 6, 79
- Strickland, D. K., Heckman, T. M., Weaver, K. A., & Dahlem, M. 2000, *AJ*, 120, 2965
- Stringer, M. J., Benson, A. J., Bundy, K., Ellis, R. S., & Quetin, E. L. 2009, *MNRAS*, 393, 1127
- Sutherland, R. S., & Dopita, M. A. 1993, *ApJS*, 88, 253
- Taffoni, G., Mayer, L., Colpi, M., & Governato, F. 2003, *MNRAS*, 341, 434
- Tegmark, M., Blanton, M. R., Strauss, M. A., et al. 2004, *ApJ*, 606, 702
- Thomas, D., Maraston, C., Bender, R., & Mendes de Oliveira, C. 2005, *ApJ*, 621, 673
- Thoul, A. A., & Weinberg, D. H. 1996, *ApJ*, 465, 608
- Tormen, G. 1997, *MNRAS*, 290, 411
- Trujillo, I., Conselice, C. J., Bundy, K., et al. 2007, *MNRAS*, 382, 109
- Trujillo, I., Cenarro, A. J., de Lorenzo-Cáceres, A., et al. 2009, *ApJ*, 692, L118
- Valentinuzzi, T., Fritz, J., Poggianti, B. M., et al. 2010, *ApJ*, 712, 226
- van Dokkum, P. G. 2005, *AJ*, 130, 2647
- Viola, M., Monaco, P., Borgani, S., Murante, G., & Tornatore, L. 2008, *MNRAS*, 383, 777
- Volonteri, M., Lodato, G., & Natarajan, P. 2008, *MNRAS*, 383, 1079
- Warren, M. S., Quinn, P. J., Salmon, J. K., & Zurek, W. H. 1992, *ApJ*, 399, 405
- Weinmann, S. M., van den Bosch, F. C., Yang, X., et al. 2006, *MNRAS*, 372, 1161
- White, S. D. M., & Rees, M. J. 1978, *MNRAS*, 183, 341
- White, S. D. M., & Frenk, C. S. 1991, *ApJ*, 379, 52
- White, S. D. M., Navarro, J. F., Evrard, A. E., & Frenk, C. S. 1993, *Nature*, 366, 429
- Zentner, A. R. 2007, *IJMPD*, 16, 763
- Zhang, J., Ma, C.-P., & Fakhouri, O. 2008, *MNRAS*, 387, L13